

# Twisted Trilayer Graphene: a Precisely Tunable Platform for Correlated Electrons

Ziyan Zhu,<sup>1</sup> Stephen Carr,<sup>1</sup> Daniel Massatt,<sup>2</sup> Mitchell Luskin,<sup>3</sup> and Efthimios Kaxiras<sup>1,4</sup>

<sup>1</sup>*Department of Physics, Harvard University, Cambridge, Massachusetts 02138, USA*

<sup>2</sup>*Department of Statistics, The University of Chicago, Chicago, Illinois 60637, USA*

<sup>3</sup>*School of Mathematics, University of Minnesota - Twin Cities, Minneapolis, Minnesota 55455, USA*

<sup>4</sup>*John A. Paulson School of Engineering and Applied Sciences, Harvard University, Cambridge, Massachusetts 02138, USA*

We introduce twisted trilayer graphene (tTLG) with two independent twist angles as an ideal system for the precise tuning of the electronic interlayer coupling to maximize the effect of correlated behaviors. As established by experiment and theory in the related twisted bilayer graphene system, van Hove singularities (VHS) in the density of states can be used as a proxy of the tendency for correlated behaviors. To explore the evolution of VHS in the twist-angle phase space of tTLG, we present a general low-energy electronic structure model for any pair of twist angles. We show that the basis of the model has infinite dimensions even at a finite energy cutoff and that no Brillouin zone exists even in the continuum limit. Using this model, we demonstrate that the tTLG system exhibits a wide range of magic angles at which VHS merge and the density of states has a sharp peak at the charge-neutrality point through two distinct mechanisms: the incommensurate perturbation of twisted bilayer graphene’s flatbands or the equal hybridization between two bilayer moiré superlattices.

*Introduction.* — Electronic properties in stacked graphene layers can be tuned by a small twist angle that modifies the interlayer interaction strength, an effect referred to as “twistronics” [1]. As the twist angle approaches a critical “magic angle” ( $\sim 1.05^\circ$  in twisted bilayer graphene), the two van Hove singularities (VHS) in the density of states (DOS) of each monolayer merge, resulting in a sharp peak associated with flatbands, leading to the emergence of strongly correlated electronic phases [2]. The small twist angle gives rise to large-scale repeating patterns, known as moiré patterns. Unconventional correlated states have now been observed in many van der Waals (vdW) heterostructures with one twist angle, e.g., twisted bilayer graphene (tBLG) and twisted double bilayer graphene [3–15]. In these systems, electrons responsible for the correlation effects localize at the moiré scale [16–18].

The addition of a third layer introduces a new degree of freedom, the second twist angle, allowing for the further tuning of electron correlations. In twisted trilayer graphene (tTLG) with two consecutive twist angles,  $\theta_{12}$  and  $\theta_{23}$ , the beating of two bilayer moiré patterns leads to higher-order patterns (moiré of moiré). The length scale of these is orders of magnitude larger than the bilayer moiré [Fig. 1(a)] [19–21]. Unlike in tBLG where only the lowest-order moiré pattern dominates in the continuum limit, the dominant harmonic is twist-angle dependent in tTLG. For a given moiré of moiré harmonic labeled by  $(m, n)$ , the primitive reciprocal lattice vectors are given as the column vectors of  $G_{mn}^H = mG_{12} - nG_{23}$ , where the matrix  $G_{ij}$  spans the bilayer moiré reciprocal space between layers  $i$  ( $Li$ ) and  $j$  ( $Lj$ ). The real space moiré of moiré supercell  $A_{mn}^H$  is obtained by  $A_{mn}^H = \frac{1}{2\pi}(G_{mn}^H)^{-T}$ , with the norm of its column vectors being the moiré of moiré length. Figure 1b shows the dominant moiré

of moiré length as a function of twist angles, in which each lobe corresponds to the region where a different harmonic  $(m, n)$  dominates. The moiré of moiré patterns can be discerned visually only near the  $(N, 1)$  or  $(1, N)$  lobes for  $N \in \mathbb{Z}$ . Generally, multiple harmonics have competing length scales (see Supplemental Material Sec. I [22]). Therefore, tTLG cannot be approximated by two aligned tBLG and a general expression for the trilayer supercell does not exist, making it fundamentally different than multilayered vdW heterostructures with a single twist angle [23–26]. The lack of a supercell approximation and the large length scale pose many computational challenges to the theoretical modeling of tTLG. While there have been some theoretical studies of tTLG [19, 27, 28], including an accurate treatment of any twist angles by Amorim and Castro [27], an electronic structure model incorporating both accuracy and efficiency is lacking; this severely restricts our ability to investigate its electronic properties and the potential for correlated phases, which have been observed recently in tTLG at the moiré of moiré scale [29].

Here, we present tTLG as a platform to precisely tune twistronic correlations, using the VHS intensity as a proxy for strong correlations. We derive a general momentum-space model to study the electronic properties of the two-independent-twist-angle tTLG system using a low-energy  $k \cdot p$  model that provides computational efficiency and removes the constraint on the twist angle in atomistic calculations with supercells. Using this model, we explore the tTLG phase space. We find that the two bilayer moiré superlattices hybridize when the two twist angles are equal, minimizing the separation between the two lowest VHS at a critical angle. At general twist angles, there exists a wide range of values at which the VHS merge and the DOS is sharply peaked at

the charge-neutrality point (CNP). These magic angles can be understood as a tBLG magic angle modified by an incommensurate perturbative potential from the third layer. Our analysis is well suited to guide experimental searches for correlation effects and enables the interpretation of otherwise unclear experimental findings [29].

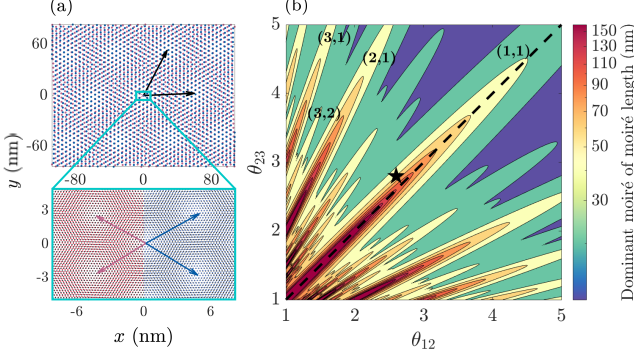


FIG. 1: Illustration of moiré of moiré pattern in tTLG for  $\theta_{12} = 2.6^\circ$ ,  $\theta_{23} = 2.8^\circ$ . Red and blue points represent the lattice points of the bilayer moiré supercells between L1-L2 and L2-L3 respectively. Black arrows represent dominant moiré of moiré supercell lattice vectors. A blowup of the small boxed area is shown below, with points representing monolayer lattice points, for L1 and L2 on the left half and for L2 and L3 on the right half. The moiré lattice vectors (red and blue arrows) are slightly rotated and have different lattice constants. (b) The dominant moiré of moiré length on a logarithmic color scale. The black star corresponds to the twist angle in (a), and  $(m, n)$  labels the dominant moiré harmonic in the nearby lobe. Black dashed line represents  $\theta_{12} = \theta_{23}$ .

*Momentum-space Hamiltonian.* — To obtain the electronic structure model for tTLG, we employ a momentum-space method by taking the Fourier transform of the real-space tight-binding model. At a momentum  $\mathbf{k}$  (referred to as the center site), the model can be formally represented by a  $3 \times 3$  block matrix:

$$\mathcal{H}(\mathbf{k}) = \begin{bmatrix} H^1(\mathbf{k}) & T^{12} & 0 \\ T^{12\dagger} & H^2(\mathbf{k}) & T^{23} \\ 0 & T^{23\dagger} & H^3(\mathbf{k}) \end{bmatrix}. \quad (1)$$

The diagonal blocks are the monolayer graphene tight-binding Hamiltonians in the rotated basis [30], representing the intralayer hopping. The off-diagonal blocks represent the interlayer hopping. The interlayer terms that connect two momentum degrees of freedom  $\mathbf{k}^{(i)}$  and  $\mathbf{k}^{(j)}$  in  $L_i$  and  $L_j$  are given as,

$$T_{\alpha\beta}^{ij}[\mathbf{k}^{(i)}, \mathbf{k}^{(j)}] = \frac{1}{|\Gamma|} \sum_{\mathbf{G}^{(i)}, \mathbf{G}^{(j)}} e^{i\mathbf{G}^{(i)} \cdot \boldsymbol{\tau}_\alpha^{(i)}} \times \tilde{t}_{\alpha\beta}^{ij}[\mathbf{k} + \mathbf{k}^{(i)} + \mathbf{G}^{(i)}] e^{-i\mathbf{G}^{(j)} \cdot \boldsymbol{\tau}_\beta^{(j)}} \delta_{\mathbf{k}^{(i)} - \mathbf{G}^{(i)}, \mathbf{k}^{(j)} - \mathbf{G}^{(j)}}, \quad (2)$$

where  $|\Gamma|$  is the monolayer unit cell area,  $\boldsymbol{\tau}_\alpha$  ( $\boldsymbol{\tau}_\beta$ ) is the position of the sublattice  $\alpha$  ( $\beta$ ),  $\mathbf{G}^{(\ell)}$  is a reciprocal space lattice vector in  $L_\ell$ , and  $\tilde{t}_{\alpha\beta}^{ij}(\mathbf{p})$  is the momentum-space hopping parameter between sublattice  $\alpha$  in  $L_i$  and sublattice  $\beta$  in  $L_j$ . The  $\delta$  function imposes the constraint on the values of  $\mathbf{k}^{(\ell)}$ , dictating the interlayer scattering selection rule. The above expressions are equivalent to a real-space tight-binding model in the Bloch basis (See Supplemental Material, Sec. IIA, for derivation [22]).

Unlike tBLG [31–35], the momentum-space basis in tTLG is infinitely dimensional and lacks a Brillouin zone even in the continuum limit. In bilayers, coupled momentum states satisfy the selection rule  $\mathbf{k}^{(1)} - \mathbf{k}^{(2)} = \mathbf{G}^{(1)} - \mathbf{G}^{(2)}$  [33]. Note that for a given  $\mathbf{G}^{(1)} = m\mathbf{b}_1^{(1)} + n\mathbf{b}_2^{(1)}$  for  $m, n \in \mathbb{Z}$ , we also have  $\mathbf{G}^{(2)} = m\mathbf{b}_1^{(2)} + n\mathbf{b}_2^{(2)}$  for the same  $m, n$ , where  $\mathbf{b}_i^{(\ell)}$  is the  $i$ -th component of the primitive reciprocal lattice vector of  $L_\ell$ , since other hopping processes are much higher in energy. As  $|\mathbf{G}^{(\ell)}|$  increases, the scattered momentum,  $\mathbf{k}'$ , becomes farther away from the Dirac point. Therefore, to implement a finite cutoff, we can simply constrain the magnitude of the scattered momentum  $\mathbf{k}' = \mathbf{G}^{(\ell)}$  for  $\ell = 1, 2$ . Physically,  $\mathbf{k}'$  is a monolayer reciprocal lattice vector that can scatter to a nearby momentum in the other layer. In contrast, in trilayers, the momentum states that form the basis of the Hamiltonian are connected in a more complicated way. A given  $\mathbf{k}^{(1)}$  can couple to a momentum state  $\mathbf{k}^{(2)}$  that satisfies  $\mathbf{k}^{(2)} = \mathbf{k}^{(1)} + \mathbf{G}^{(2)} - \mathbf{G}^{(1)}$ , same as in bilayers. Each  $\mathbf{k}^{(2)}$  can then couple to a momentum state  $\mathbf{k}^{(3)}$  through the second selection rule [Eq. (2)], resulting in the following final momentum:

$$\mathbf{k}^{(3)} = \mathbf{k}^{(1)} + [\mathbf{G}^{(2)} - \mathbf{G}^{(1)}] + [\mathbf{G}^{(3)} - \mathbf{G}^{(2)}], \quad (3)$$

where the reciprocal lattice vectors satisfy  $\mathbf{G}^{(2)} - \mathbf{G}^{(1)} = m\mathbf{b}_1^{(12)} + n\mathbf{b}_2^{(12)}$  and  $\mathbf{G}^{(3)} - \mathbf{G}^{(2)} = m'\mathbf{b}_1^{(23)} + n'\mathbf{b}_2^{(23)}$  for  $m, n, n', m' \in \mathbb{Z}$ , with  $\mathbf{b}_k^{(ij)} = \mathbf{b}_k^{(j)} - \mathbf{b}_k^{(i)}$  being the bilayer moiré reciprocal space lattice vectors. Equation (3) suggests that L1 and L3 are coupled through L2, even though a direct interlayer hopping is not allowed. Unlike the simple 2D momentum crystal in bilayers, here the incommensuration between  $\mathbf{b}_k^{(12)}$  and  $\mathbf{b}_k^{(23)}$  creates for  $\mathbf{k}^{(3)}$  a 4D structure that is projected onto 2D.

Equation (3) suggests that in  $L_\ell$  of tTLG,  $\mathbf{k}'$  is given by  $\mathbf{k}' = \mathbf{G}^{(i)} + \mathbf{G}^{(j)}$  for  $\ell \neq i, j$ . To implement a cutoff, we should impose  $|\mathbf{k}'| \leq k_c$  for some cutoff value  $k_c$ . However, the incommensurability of twisted trilayers suggests that  $|\mathbf{k}'|$  can be arbitrarily small and imposing  $|\mathbf{k}'| \leq k_c$  still leads to an infinite basis. For example, in Fig. 2(a), even though  $\mathbf{G}^{(2)}$  lies outside of the cutoff, the resulting  $\mathbf{k}'$  is still a relevant low-energy degree of freedom, due to the two-step scattering process. A similar construction can be made for all other  $\mathbf{G}^{(2)}$  outside of the cutoff radius, which means within a finite cutoff, there are infinitely many coupled momentum states. In practice,

another set of cutoff conditions needs to be implemented, namely  $|\mathbf{G}^{(\ell)}| \leq k_c$ . With the constraint on  $|\mathbf{G}^{(\ell)}|$ , the  $\mathbf{k}'$  in Fig. 2(a) is no longer allowed. In this way, we ignore the cases where  $|\mathbf{G}^{(\ell)}|$  is large but  $|\mathbf{k}'|$  is small, leading to the neglect of some low-energy degrees of freedom and hence convergence is not guaranteed, which merits future work (see Supplemental Material, Sec. IID, for convergence study [22]). In this work, we choose  $k_c = 4|\mathbf{b}^{(\ell)}|$ , with  $\sim 5600$  momenta, such that the properties of interest (e.g., DOS maximum and the VHS location) do not change significantly as  $k_c$  increases.

We take the low-energy limit by expanding around the Dirac point of each layer,  $K_{L\ell}$ , letting  $\mathbf{k}^{(\ell)} = \mathbf{q}^{(\ell)} + K_{L\ell}$ , which simplifies the model proposed by Amorim and Castro [27]. The intralayer Hamiltonian becomes the rotated Dirac equation,  $H^\ell = v_F \mathbf{q} \cdot (\sigma_x^{\theta_\ell}, -\sigma_y^{\theta_\ell})$ , where  $\sigma_x^{\theta_\ell} = \sigma_x \cos \theta_\ell - \sigma_y \sin \theta_\ell$  and  $\sigma_y^{\theta_\ell} = \sigma_x \sin \theta_\ell + \sigma_y \cos \theta_\ell$  are rotated Pauli matrices with  $\theta_1 = \theta_{12}, \theta_2 = 0, \theta_3 = -\theta_{23}$ ,  $v_F = 0.8 \times 10^6$  cm/s is the Fermi velocity [36], and  $\mathbf{q} = \mathbf{k} + \mathbf{k}^{(\ell)} - K_{L\ell}$ . For the interlayer hopping, we make the approximation that  $\tilde{t}_{\alpha\beta}^{ij}[\mathbf{k} + \mathbf{k}^{(i)} + \mathbf{G}^{(i)}] \approx \tilde{t}_{\alpha\beta}^{ij}[\mathbf{G}^{(i)} + K_{Li}]$  since  $|\mathbf{k}|, |\mathbf{q}^{(i)}| \ll |K_{Li}|, |\mathbf{G}^{(i)}|$ , for  $\mathbf{k}$  near the Dirac point. Due to the rapid decay of  $\tilde{t}_{\alpha\beta}^{ij}(\mathbf{p})$  as  $\mathbf{p}$  increases [2, 36, 37], we keep only the first shell in the summation in Eq. (2):

$$T_{\alpha\beta}^{ij}[\mathbf{q}^{(i)}, \mathbf{q}^{(j)}] = \sum_{n=1}^3 T_{n,\alpha\beta}^{ij} \delta_{\mathbf{q}^{(i)} - \mathbf{q}^{(j)}, -\mathbf{q}_n^{ij}}, \quad (4)$$

where  $\mathbf{q}_1^{ij} = K_{Li} - K_{Lj}$ ,  $\mathbf{q}_2^{ij} = \mathcal{R}^{-1}(2\pi/3)\mathbf{q}_1^{ij}$ , and  $\mathbf{q}_3^{ij} = \mathcal{R}(2\pi/3)\mathbf{q}_1^{ij}$  using a counterclockwise rotation matrix  $\mathcal{R}(\theta)$ . We include out-of-plane relaxation by letting  $t_{AA}^{ij} = t_{BB}^{ij} = \omega_0 = 0.07$  eV and  $t_{AB}^{ij} = t_{BA}^{ij} = \omega_1 = 0.11$  eV [32, 38]. In the matrix form,

$$T_1^{ij} = \begin{bmatrix} \omega_0 & \omega_1 \\ \omega_1 & \omega_0 \end{bmatrix}, T_2^{ij} = \begin{bmatrix} \omega_0 & \omega_1 \bar{\phi} \\ \omega_1 \phi & \omega_0 \end{bmatrix}, T_3^{ij} = \bar{T}_2^{ij}, \quad (5)$$

where  $\phi = \exp(i2\pi/3)$  and  $\bar{z}$  indicates the complex conjugate of  $z$ . In tBLG, with the low-energy expansion, momenta  $\mathbf{q}^{(1)}$  and  $\mathbf{q}^{(2)}$  form a hexagonal lattice with the neighboring hexagon corners representing states from alternating layers (a moiré momentum lattice) [2, 33]. In tTLG, on top of each lattice point of the L1-L2 moiré momentum lattice, the additional scattering process creates a copy of the L2-L3 moiré momentum lattice (Fig. 2b), suggesting the absence of a Brillouin zone.

*Density of states* — We use Gaussian smearing to obtain the total DOS, summing over the two bilayer moiré Brillouin zones, each discretized using a  $22 \times 22$  grid [39] (see Supplemental Material Sec. IIC for the expression [22]). For normalization, we first calculate the DOS of only the intralayer Hamiltonian, which reduces to three independent copies of monolayer graphene [30]. We then obtain the normalization constant by fixing the prefactor to the expected low-energy monolayer DOS and

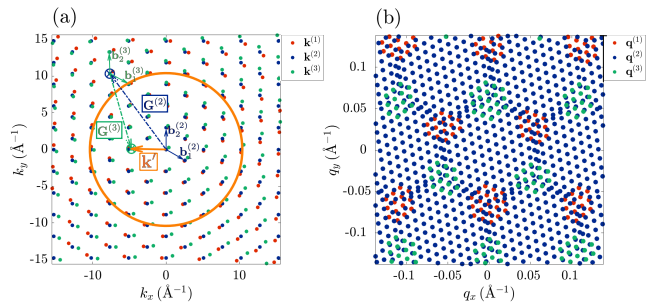


FIG. 2: Momentum degrees of freedom for tTLG at  $\theta_{12} = 2.2^\circ, \theta_{23} = 2^\circ$ . Red, blue, and green are the reciprocal lattice vectors of L1, L2, and L3 respectively. The origin is the Dirac point of L2. (a) Extended zone scheme, with the orange circle indicating the cutoff in  $|\mathbf{k}'|$ .  $\mathbf{k}' = \mathbf{G}^{(2)} + \mathbf{G}^{(3)}$  falls within the cutoff radius  $10\text{\AA}^{-1}$  despite both  $|\mathbf{G}^{(2)}|$  and  $|\mathbf{G}^{(3)}|$  being large. The momenta of L3 are centered at  $\mathbf{G}^{(2)}$ . (b) Reduced zone scheme, folded back to the monolayer Dirac points,  $\mathbf{q}^{(\ell)} = \mathbf{k}^{(\ell)} - K_{L\ell}$ . This basis corresponds to the same twist angle as (a) but with an additional constraint  $|\mathbf{G}^{(\ell)}| \leq k_c = 6|\mathbf{b}^{(\ell)}|$ , leading to 26921 momenta.

using the same constant for the DOS of the full Hamiltonian. We adapt the Gaussian FWHM,  $\kappa$ , based on the twist angle  $\theta_{\ell,\ell+1}$ : for  $\theta_{\ell,\ell+1} \leq 2^\circ$ ,  $\kappa = 0.35$  meV; for  $\theta_{\ell,\ell+1} \in (2^\circ, 3.9^\circ]$ ,  $\kappa = 1.2$  meV; for  $\theta_{\ell,\ell+1} > 3.9^\circ$ ,  $\kappa = 2.4$  meV.

*Evolution of VHS.* — We explore next the behavior of VHS as a function of twist angles in tTLG, by investigating the DOS enhancement and the narrowing of the separation between VHS (referred to as the VHS gap). We define a magic angle approximately as a geometry where both features are achieved. Figure 3(a) shows the DOS of tTLG at  $\theta_{12} = \theta_{23}$ . The bright regions represent VHS. As the twist angle decreases, the VHS gap first decreases and then increases after reaching a minimum at  $\sim 2.1^\circ$ . This behavior is similar to the evolution of VHS in tBLG in which changing the twist angle tunes the hybridization between two monolayer Dirac cones. In tTLG with  $\theta_{12} = \theta_{23}$ , varying the twist angle changes the hybridization strength between the two identical bilayer moiré superlattices. However, the two VHS can never merge at the CNP, with the minimum VHS gap being  $\sim 20$  meV at  $2.1^\circ$ . The DOS is also orders of magnitude lower than at the tBLG magic angle. For general twist angles, Fig. 3(b) shows the DOS as a function of  $\theta_{12}$  with  $\theta_{23} = 3^\circ$ . Unlike when  $\theta_{12} = \theta_{23}$ , the two VHS approach each other as the twist angle decreases and merge when  $1.3^\circ \leq \theta_{12} \leq 1.6^\circ$ , resulting in a sharp DOS peak.

To investigate the nature of DOS enhancements in tTLG, we performed calculations over an entire region of the  $\theta_{12}, \theta_{23}$  parameter space. Figure 4 shows the DOS maximum and the VHS gap,  $\Delta E$ , as a function of both twist angles [40]. The magic-angle condition is met at a wide range of twist angles that follows a smooth curve but

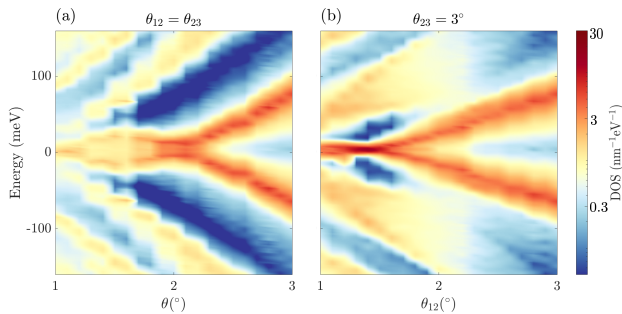


FIG. 3: (a) DOS as a function of twist angle for  $\theta_{12} = \theta_{23}$ . (b) DOS as a function  $\theta_{12}$  at  $\theta_{23} = 3^\circ$ , both on a logarithmic color scale.

disappears near the diagonal. Although there is no significant DOS enhancement at  $\theta_{12} = \theta_{23}$ , the DOS maximum is higher compared to the nearby regions where  $\theta_{12}$  and  $\theta_{23}$  differ slightly [light yellow region within the dotted lines in Fig. 4(a)].

We now examine the magic angles away from the diagonal. In the limit where  $\theta_{12} \gg \theta_{23}$  or  $\theta_{12} \ll \theta_{23}$ , tTLG decomposes into a decoupled tBLG moiré supercell and a graphene monolayer; the monolayer does not contribute significantly to the low-energy features. Therefore, we observe that the tTLG magic-angle curve asymptotically approaches the tBLG magic angle [dashed lines in Fig. 4(a)] for large  $\theta_{12}$  or  $\theta_{23}$ . We verified numerically that when one twist angle is very large,  $\theta_{12} = 40^\circ$  for instance, the DOS maximum occurs exactly when  $\theta_{23}$  is at the tBLG magic angle. The continuous curve and its asymptotic behavior suggest that these magic angles can be understood as the magic-angle tBLG modified by an effective potential,  $V$ , from the third layer. We can qualitatively analyze this argument using perturbation theory, by truncating the momentum space to the first shell, including one state from L2 and three states each from L1 and L3. We obtain the renormalized Fermi velocity  $v_F^*$  by extracting the coefficient of the first-order effective Hamiltonian in  $\mathbf{q}$  in the form of a Dirac Hamiltonian, given by

$$v_F^* = \frac{1 - 3(\alpha_{12}^2 + \alpha_{23}^2)}{1 + 6(\alpha_{12}^2 + \alpha_{23}^2)} v_F, \quad (6)$$

where  $\alpha_{ij} = \omega / (v_F k_{\theta_{ij}})$ ,  $k_{\theta_{ij}} = 8\pi \sin(\theta_{ij}/2) / (3a_G)$ , assuming that  $\omega_0 = \omega_1 = \omega$ . The Hamiltonian and its derivation are provided in Section III of the Supplemental Material [22]. Magic angles occur when  $v_F^*$  vanishes, leading to the following condition:

$$\alpha_{12}^2 + \alpha_{23}^2 = \frac{1}{3}. \quad (7)$$

The solid line in Fig. 4(a) corresponds to  $\theta_{12}$  and  $\theta_{23}$  that satisfy Eq. (7), which matches the DOS peaks and  $\Delta E$  minima in Fig. 4(a), (b). Taking the large angle limit,

for example, when  $\theta_{23} \rightarrow \infty$ ,  $\alpha_{23} \rightarrow 0$ , Eq. (7) becomes  $\alpha_{12}^2 = \frac{1}{3}$ , which is the tBLG magic-angle condition [2].

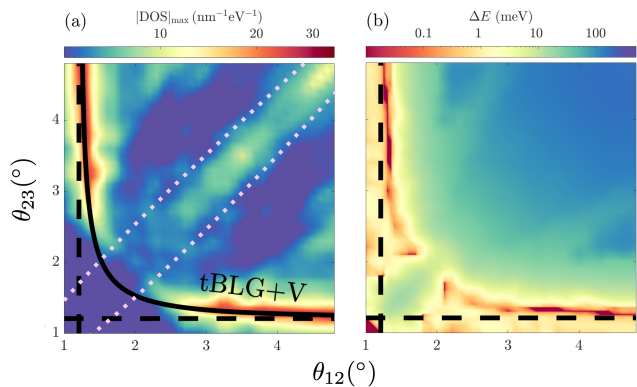


FIG. 4: (a) DOS maximum and (b) VHS gap,  $\Delta E$ , as a function of twist angles on a logarithmic color scale. The black solid line follows the tTLG magic angles predicted by Eq. (7). Vertical and horizontal black dashed lines correspond to  $\theta_{12}$  and  $\theta_{23}$  at the tBLG magic angle respectively. Within the dotted lines is roughly the region that can be understood as the hybridization between two bilayer moiré superlattices.

The evolution of VHS along the diagonal likely has a different origin than the magic angles for  $\theta_{12} \neq \theta_{23}$ . Perturbation theory predicts that  $v_F^*$  can reach 0 at  $\theta_{12} = \theta_{23} = 1.72^\circ$ . In the numerical calculations, however, we do not observe  $v_F^* = 0$  at equal twist angles, and the twist angle with the minimal VHS gap ( $2.1^\circ$ ) deviates from the perturbation theory prediction. The discrepancy suggests that the perturbation argument does not apply to equal twist angles, since features near the diagonal are more aptly described by the hybridization between the two bilayer moiré superlattices with a shared middle layer, rather than between two independent unit cells as in tBLG.

*Moiré of moiré.* — In magic-angle tBLG, correlated states occur at the half-filling of the moiré supercell by filling two isolated flatbands [3, 4, 16–18]. In tTLG, even though the origin of some magic angles is perturbed tBLG, filling each flatband corresponds to filling the moiré of moiré supercell rather than the bilayer moiré cell because the incommensurate effective potential modifies the relevant supercell area.

We compare our results to a simplified model that approximates tTLG as two aligned moiré cells [28]. While we observe similar qualitative behaviors, the simplified model fails to capture physics at the moiré of moiré scale and does not predict as drastic a DOS enhancement as our work. Moreover, the simplified model requires a new basis for different sets of twist angles, making it difficult to generalize – limitations that our model overcomes. We include a comparison between the two models in Section IV of the Supplemental Material IV [22].

In summary, we explore the rich electronic behavior

of tTLG in its twist-angle phase space. We offer a general low-energy momentum-space model to obtain electronic structure in tTLG. We show that the twisted trilayer momentum-space model does not have a Brillouin zone and has an infinitely sized basis. Although we do not predict correlation strengths directly, we can use the presence of VHS as a proxy for electronic correlation. We show that the tTLG system exhibits a wide range of magic angles with merging VHS at the CNP. Away from equal twist angles, the origin of the magic angles can be understood as tBLG in an incommensurate perturbative potential. At equal twist angles, the electronic properties are a result of the hybridization between two bilayer moiré superlattices that share the middle layer. Tuning the twist angle makes it possible to traverse between these two regimes. Our MATLAB code for the model is openly available [41].

We thank Ke Wang, Xi Zhang, Kan-Ting Tsai, Francisco Guinea, Philip Kim, and Paul Cazeaux for helpful discussions. This work was supported by the STC Center for Integrated Quantum Materials, NSF Grant No. DMR-1231319, ARO MURI Grant No. W911NF-14-0247, and NSF DMREF Grant No. 1922165. Calculations were performed on the Odyssey cluster supported by the FAS Division of Science, Research Computing Group at Harvard University.

- 
- [1] Stephen Carr, Daniel Massatt, Shiang Fang, Paul Cazeaux, Mitchell Luskin, and Efthimios Kaxiras, “Twistronics: Manipulating the electronic properties of two-dimensional layered structures through their twist angle,” *Phys. Rev. B* **95**, 075420 (2017).
- [2] Rafi Bistritzer and Allan H. MacDonald, “Moiré bands in twisted double-layer graphene,” *Proceedings of the National Academy of Science* **108**, 12233–12237 (2011).
- [3] Yuan Cao, Valla Fatemi, Ahmet Demir, Shiang Fang, Spencer L. Tomarken, Jason Y. Luo, Javier D. Sanchez-Yamagishi, Kenji Watanabe, Takashi Taniguchi, Efthimios Kaxiras, Ray C. Ashoori, and Pablo Jarillo-Herrero, “Correlated insulator behaviour at half-filling in magic-angle graphene superlattices,” *Nature (London)* **556**, 80–84 (2018).
- [4] Yuan Cao, Valla Fatemi, Shiang Fang, Kenji Watanabe, Takashi Taniguchi, Efthimios Kaxiras, and Pablo Jarillo-Herrero, “Unconventional superconductivity in magic-angle graphene superlattices,” *Nature (London)* **556**, 43–50 (2018).
- [5] Guorui Chen, Lili Jiang, Shuang Wu, Bosai Lyu, Hongyuan Li, Bheema Lingam Chittari, Kenji Watanabe, Takashi Taniguchi, Zhiwen Shi, Jeil Jung, Yuanbo Zhang, and Feng Wang, “Evidence of a gate-tunable Mott insulator in a trilayer graphene moiré superlattice,” *Nature Physics* **15**, 237–241 (2019).
- [6] Matthew Yankowitz, Jeil Jung, Evan Laksono, Nicolas Leconte, Bheema L. Chittari, K. Watanabe, T. Taniguchi, Shaffique Adam, David Graf, and Cory R. Dean, “Dynamic band-structure tuning of graphene moiré superlattices with pressure,” *Nature (London)* **557**, 404–408 (2018).
- [7] Matthew Yankowitz, Shaowen Chen, Hryhorii Polshyn, Yuxuan Zhang, K. Watanabe, T. Taniguchi, David Graf, Andrea F. Young, and Cory R. Dean, “Tuning superconductivity in twisted bilayer graphene,” *Science* **363**, 1059–1064 (2019).
- [8] Cheng Shen, Na Li, Shuopei Wang, Yanchong Zhao, Jian Tang, Jieying Liu, Jinpeng Tian, Yanbang Chu, Kenji Watanabe, Takashi Taniguchi, Rong Yang, Zi Yang Meng, Dongxia Shi, and Guangyu Zhang, “Correlated states in twisted double bilayer graphene,” *Nature Physics* **16**, 520–525 (2020).
- [9] Xiaomeng Liu, Zeyu Hao, Eslam Khalaf, Jong Yeon Lee, Yuval Ronen, Hyobin Yoo, Danial Haei Najafabadi, Kenji Watanabe, Takashi Taniguchi, Ashvin Vishwanath, *et al.*, *Nature* **583**, 221–225 (2020).
- [10] Yuan Cao, Daniel Rodan-Legrain, Oriol Rubies-Bigorda, Jeong Min Park, Kenji Watanabe, Takashi Taniguchi, and Pablo Jarillo-Herrero, “Electric Field Tunable Correlated States and Magnetic Phase Transitions in Twisted Bilayer-Bilayer Graphene,” *Nature*, 1–6 (2020).
- [11] G. William Burg, Jihang Zhu, Takashi Taniguchi, Kenji Watanabe, Allan H. MacDonald, and Emanuel Tutuc, “Correlated insulating states in twisted double bilayer graphene,” *Phys. Rev. Lett.* **123**, 197702 (2019).
- [12] Lei Wang, En-Min Shih, Augusto Ghiotto, Lede Xian, Daniel A. Rhodes, Cheng Tan, Martin Claassen, Dante M. Kennes, Yusong Bai, Bumho Kim, Kenji Watanabe, Takashi Taniguchi, Xiaoyang Zhu, James Hone, Angel Rubio, Abhay Pasupathy, and Cory R. Dean, “Magic continuum in twisted bilayer WSe<sub>2</sub>,” arXiv e-prints, arXiv:1910.12147 (2019), arXiv:1910.12147 [cond-mat.mes-hall].
- [13] Yu Saito, Jingyuan Ge, Kenji Watanabe, Takashi Taniguchi, and Andrea F. Young, “Decoupling superconductivity and correlated insulators in twisted bilayer graphene,” arXiv e-prints, arXiv:1911.13302 (2019), arXiv:1911.13302 [cond-mat.mes-hall].
- [14] Zhiming Zhang, Rachel Myers, Kenji Watanabe, Takashi Taniguchi, and Brian J. LeRoy, “Probing the wavefunctions of correlated states in magic angle graphene,” arXiv e-prints, arXiv:2003.09482 (2020), arXiv:2003.09482 [cond-mat.mes-hall].
- [15] Xiaoxue Liu, Zhi Wang, K. Watanabe, T. Taniguchi, Oskar Vafek, and J. I. A. Li, “Tuning electron correlation in magic-angle twisted bilayer graphene using Coulomb screening,” arXiv e-prints, arXiv:2003.11072 (2020), arXiv:2003.11072 [cond-mat.mes-hall].
- [16] Mikito Koshino, Noah F. Q. Yuan, Takashi Koretsune, Masayuki Ochi, Kazuhiko Kuroki, and Liang Fu, “Maximally Localized Wannier Orbitals and the Extended Hubbard Model for Twisted Bilayer Graphene,” *Physical Review X* **8**, 031087 (2018).
- [17] Hoi Chun Po, Liujun Zou, T. Senthil, and Ashvin Vishwanath, “Faithful tight-binding models and fragile topology of magic-angle bilayer graphene,” *Phys. Rev. B* **99**, 195455 (2019).
- [18] Stephen Carr, Shiang Fang, Hoi Chun Po, Ashvin Vishwanath, and Efthimios Kaxiras, “Derivation of Wannier orbitals and minimal-basis tight-binding Hamiltonians for twisted bilayer graphene: First-principles approach,” *Physical Review Research* **1**, 033072 (2019).
- [19] Ziyang Zhu, Paul Cazeaux, Mitchell Luskin, and

- Efthimios Kaxiras, “Modeling mechanical relaxation in incommensurate trilayer van der waals heterostructures,” *Phys. Rev. B* **101**, 224107 (2020).
- [20] M. Andelković, S. P. Milovanović, L. Covaci, and F. M. Peeters, “Double moiré with a twist: super-moiré in encapsulated graphene,” *Nano Letters* **20**, 979–988 (2020).
- [21] N Leconte and J Jung, “Commensurate and incommensurate double moire interference in graphene encapsulated by hexagonal boron nitride,” *2D Materials* **7**, 031005 (2020).
- [22] See Supplemental Material for the calculation of moiré of moiré length, a detailed derivation of the momentum space model and convergence test, the derivation of the analytical expression of the tTLG magic angles, and comparisons with other models, which includes Refs. [42, 43].
- [23] Xiao Li, Fengcheng Wu, and Allan H. MacDonald, “Electronic Structure of Single-Twist Trilayer Graphene,” arXiv e-prints, arXiv:1907.12338 (2019), arXiv:1907.12338 [cond-mat.mtrl-sci].
- [24] Stephen Carr, Chenyuan Li, Ziyang Zhu, Efthimios Kaxiras, Subir Sachdev, and Alexander Kruchkov, “Ultra-heavy and ultrarelativistic dirac quasiparticles in sandwiched graphenes,” *Nano Letters* **20**, 3030–3038 (2020).
- [25] Shaowen Chen, Minhao He, Ya-Hui Zhang, Valerie Hsieh, Zaiyao Fei, K. Watanabe, T. Taniguchi, David H. Cobden, Xiaodong Xu, Cory R. Dean, and Matthew Yankowitz, “Electrically tunable correlated and topological states in twisted monolayer-bilayer graphene,” arXiv e-prints, arXiv:2004.11340 (2020), arXiv:2004.11340 [cond-mat.mes-hall].
- [26] Youngju Park, Bheema Lingam Chittari, and Jeil Jung, “Gate-tunable topological flat bands in twisted monolayer-bilayer graphene,” *Phys. Rev. B* **102**, 035411 (2020).
- [27] B. Amorim and Eduardo V. Castro, “Electronic spectral properties of incommensurate twisted trilayer graphene,” arXiv e-prints, arXiv:1807.11909 (2018), arXiv:1807.11909 [cond-mat.mes-hall].
- [28] Christophe Mora, Nicolas Regnault, and B. Andrei Bernevig, “Flatbands and Perfect Metal in Trilayer Moiré Graphene,” *Phys. Rev. Lett.* **123**, 026402 (2019).
- [29] Kan-Ting Tsai, Xi Zhang, Ziyang Zhu, Yujie Luo, Stephen Carr, Mitchell Luskin, Efthimios Kaxiras, and Ke Wang, “Correlated Superconducting and Insulating States in Twisted Trilayer Graphene Moiré of Moiré Superlattices,” arXiv e-prints, arXiv:1912.03375 (2019), arXiv:1912.03375 [cond-mat.mes-hall].
- [30] A. H. Castro Neto, F. Guinea, N. M. R. Peres, K. S. Novoselov, and A. K. Geim, “The electronic properties of graphene,” *Reviews of Modern Physics* **81**, 109–162 (2009).
- [31] Nguyen N. T. Nam and Mikito Koshino, “Lattice relaxation and energy band modulation in twisted bilayer graphene,” *Phys. Rev. B* **96**, 075311 (2017).
- [32] Stephen Carr, Shiang Fang, Ziyang Zhu, and Efthimios Kaxiras, “Exact continuum model for low-energy electronic states of twisted bilayer graphene,” *Physical Review Research* **1**, 013001 (2019).
- [33] Shiang Fang, Stephen Carr, Ziyang Zhu, Daniel Massatt, and Efthimios Kaxiras, “Angle-Dependent *Ab initio* Low-Energy Hamiltonians for a Relaxed Twisted Bilayer Graphene Heterostructure,” arXiv e-prints, arXiv:1908.00058 (2019), arXiv:1908.00058 [cond-mat.mes-hall].
- [34] Francisco Guinea and Niels R. Walet, “Continuum models for twisted bilayer graphene: Effect of lattice deformation and hopping parameters,” *Phys. Rev. B* **99**, 205134 (2019).
- [35] Nicolas Leconte, Srivani Javvaji, Jiaqi An, and Jeil Jung, “Relaxation Effects in Twisted Bilayer Graphene: a Multi-Scale Approach,” arXiv e-prints, arXiv:1910.12805 (2019), arXiv:1910.12805 [cond-mat.mes-hall].
- [36] Shiang Fang and Efthimios Kaxiras, “Electronic structure theory of weakly interacting bilayers,” *Phys. Rev. B* **93**, 235153 (2016).
- [37] Gonçalo Catarina, Bruno Amorim, Eduardo V Castro, João MVP Lopes, and Nuno Peres, “Twisted bilayer graphene: Low-energy physics, electronic and optical properties,” *Handbook of Graphene, Volume 3: Graphene-like 2D Materials*, 177 (2019).
- [38] Nguyen N. T. Nam and Mikito Koshino, “Lattice relaxation and energy band modulation in twisted bilayer graphene,” *Phys. Rev. B* **96**, 075311 (2017).
- [39] Daniel Massatt, Stephen Carr, Mitchell Luskin, and Christoph Ortner, “Incommensurate heterostructures in momentum space,” *Multiscale Modeling & Simulation* **16**, 429–451 (2018).
- [40] The data set consists of a  $43 \times 43$  sampling. A Gaussian convolution kernel is applied for smoothening.
- [41] Ziyang Zhu, Carr Stephen, Massatt Daniel, Luskin Mitchell, and Kaxiras Efthimios, “Model for Twisted Trilayer Graphene: a precisely tunable platform for correlated electrons: <https://github.com/ziyazzhu/ttlg>,” (2020).
- [42] Matthew Yankowitz, Jiamin Xue, Daniel Cormode, Javier D. Sanchez-Yamagishi, K. Watanabe, T. Taniguchi, Pablo Jarillo-Herrero, Philippe Jacquod, and Brian J. Leroy, “Emergence of superlattice Dirac points in graphene on hexagonal boron nitride,” *Nature Physics* **8**, 382–386 (2012).
- [43] Wei-Jie Zuo, Jia-Bin Qiao, Dong-Lin Ma, Long-Jing Yin, Gan Sun, Jun-Yang Zhang, Li-Yang Guan, and Lin He, “Scanning tunneling microscopy and spectroscopy of twisted trilayer graphene,” *Physical Review B* **97**, 035440 (2018).

# Supplemental Material for “Twisted Trilayer Graphene: a Precisely Tunable Platform for Correlated Electrons”

Ziyan Zhu,<sup>1</sup> Stephen Carr,<sup>1</sup> Daniel Massatt,<sup>2</sup> Mitchell Luskin,<sup>3</sup> and Efthimios Kaxiras<sup>1,4</sup>

<sup>1</sup>*Department of Physics, Harvard University, Cambridge, Massachusetts 02138, USA*

<sup>2</sup>*Department of Statistics, The University of Chicago, Chicago, Illinois 60637, USA*

<sup>3</sup>*School of Mathematics, University of Minnesota - Twin Cities, Minneapolis, Minnesota 55455, USA*

<sup>4</sup>*John A. Paulson School of Engineering and Applied Sciences, Harvard University, Cambridge, Massachusetts 02138, USA*

The Supplemental Material includes four sections. In Section I, we discuss the geometry of the twisted trilayer graphene (tTLG) and calculate the higher-order moiré of moiré lengths. In Section II, we present a detailed derivation of the momentum-space model and test its convergence. In Section III, we derive analytically the magic angles in tTLG. Finally, in Section IV, we compare and contrast our results with a simplified model proposed by Mora *et al.* [S1] as well as results obtained with a full model without the low-energy expansion proposed by Amorim and Castro [S2].

## I. CALCULATION OF MOIRÉ OF MOIRÉ LENGTHS

The atomic and reciprocal space geometry of tTLG with two independent twist angles are shown in Fig. S1(a). The monolayer lattice vectors are defined as the column vectors of the following matrix:

$$A_0 = a_G \begin{bmatrix} 1 & 1/2 \\ 0 & \sqrt{3}/2 \end{bmatrix} = [\mathbf{a}_1 \quad \mathbf{a}_2], \quad (\text{S1})$$

where  $a_G = 2.4768 \text{ \AA}$  is the graphene lattice constant (as obtained from DFT). The  $l$ -th layer will be referred to as  $L\ell$ . We assume that  $L2$  is unrotated, with  $L1$  rotated clockwise by  $\theta_{12}$  and  $L3$  rotated counterclockwise by  $\theta_{23}$ . Defining the counterclockwise rotation matrix

$$\mathcal{R}(\theta) = \begin{bmatrix} \cos \theta & -\sin \theta \\ \sin \theta & \cos \theta \end{bmatrix}, \quad (\text{S2})$$

the lattice vectors of the three layers can be written as  $A_1 = \mathcal{R}(-\theta_{12})A_0$ ,  $A_2 = A_0$ , and  $A_3 = \mathcal{R}(\theta_{23})A_0$  respectively, with the column vectors denoted as  $\mathbf{a}_i^{(\ell)}$  for  $\ell = 1, 2, 3$  and  $i = 1, 2$ . The monolayer reciprocal lattice vectors are given by the columns of  $G_\ell = 2\pi A_\ell^{-T}$ . For example, the reciprocal lattice vectors of  $L2$  are  $\mathbf{b}_1^{(2)} = 2\pi/a_G(1, -\sqrt{3}/3)$  and  $\mathbf{b}_2^{(2)} = 2\pi/a_G(0, 2/\sqrt{3})$ . The K point of  $L2$  is given as  $K_{L2} = (2\mathbf{b}^{(2)} + \mathbf{b}^{(1)})/3 = (4\pi/(3a_G), 0)$ . The reciprocal lattice vectors of layers  $L1$  and  $L3$  can be obtained by acting  $\mathcal{R}(-\theta_{12})$  and  $\mathcal{R}(\theta_{23})$  on  $\mathbf{b}^{(i)}$  for  $i = 1, 2$ . We also denote the monolayer unit cell of layer  $\ell$  to be  $\Gamma^{(\ell)}$  and the reciprocal space to be  $\Gamma^{(\ell)*}$ .

The twisted trilayer system exhibits higher order moiré of moiré patterns due to the interference between the two bilayer moiré patterns. To the lowest order, the bilayer moiré length between layers  $i$  and  $j$  is given by  $a_M^{ij} = a_G/\sin \theta_{ij}$ . We denote the bilayer moiré superlattice between layers  $ij$  to be  $\Gamma^{ij}$ , spanned by the column vectors of matrix  $A_{ij} = (\mathbf{a}_1^{(ij)} \quad \mathbf{a}_2^{(ij)})$ . The bilayer moiré Brillouin zone between layers  $i$  and  $j$  are given by the column vectors of  $G_{ij} = G_j - G_i = 2\pi(A_j^{-T} - A_i^{-T})$ . The lattice vector of the moiré superlattice is the column vectors of  $A_{ij} = 2\pi G_{ij}^{-T}$ . After some algebra, we obtain the lattice vectors for the two bilayer supercells,  $\mathbf{a}_i^{12}, \mathbf{a}_i^{23}$  for  $i = 1, 2$ :

$$\begin{aligned} \mathbf{a}_1^{12} &= \frac{a_G}{2(1 - \cos \theta_{12})} [(1 - \cos \theta_{12})\hat{x} - \sin \theta_{12}\hat{y}], \\ \mathbf{a}_2^{12} &= \frac{a_G}{2(1 - \cos \theta_{12})} \left[ \left( \frac{1 - \cos \theta_{12}}{2} + \frac{\sqrt{3}}{2} \sin \theta_{12} \right) \hat{x} + \left( -\frac{1}{2} \sin \theta_{12} + \frac{\sqrt{3}}{2} (1 - \cos \theta_{12}) \right) \hat{y} \right], \\ \mathbf{a}_1^{23} &= \frac{a_G}{2(1 - \cos \theta_{23})} [(1 - \cos \theta_{23})\hat{x} + \sin \theta_{23}\hat{y}], \\ \mathbf{a}_2^{23} &= \frac{a_G}{2(1 - \cos \theta_{23})} \left[ \left( \frac{1 - \cos \theta_{23}}{2} - \frac{\sqrt{3}}{2} \sin \theta_{23} \right) \hat{x} + \left( \frac{1}{2} \sin \theta_{23} + \frac{\sqrt{3}}{2} (1 - \cos \theta_{23}) \right) \hat{y} \right]. \end{aligned} \quad (\text{S3})$$

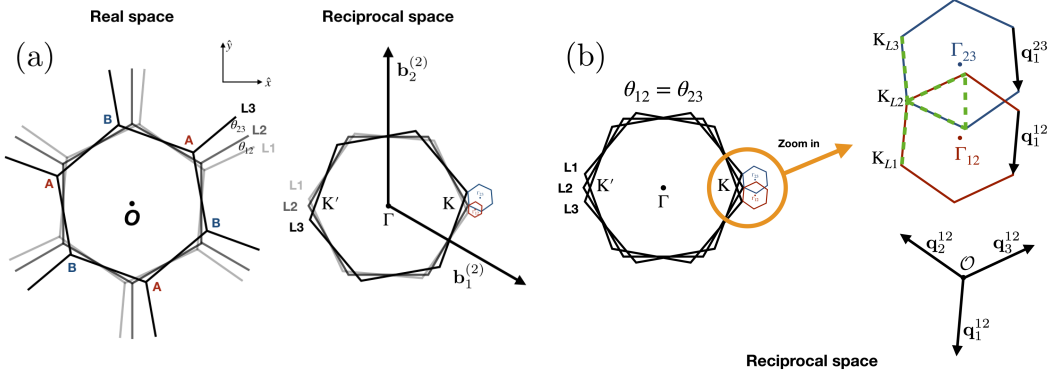


FIG. S1: Lattice geometries of the tTLG system. (a) The twisted trilayer graphene system in real space (left) and momentum space with their original monolayer reciprocal lattice vectors (right). (b) Bilinear moiré Brillouin zone for  $\theta_{12} = \theta_{23}$  with high symmetry points

Note that there is a small twist angle between the two bilayer moiré superlattices. Moreover, for general twist angles  $\theta_{12} \neq \theta_{23}$ , the two bilayer moiré cells have a lattice mismatch. The twist angle  $\phi$  and the lattice mismatch  $\delta$  between the two bilayer moiré patterns give rise to higher-order moiré of moiré lengths. The primitive reciprocal lattice vectors of a given harmonic  $(m, n)$  are given as the column vectors of  $G_{mn}^H = mG_{12} - nG_{23}$ . Inverting  $G_{mn}^H$ , we obtain the moiré of moiré supercell in real space  $A_{mn}^H = \frac{1}{2\pi}(G_{mn}^H)^{-T}$ . The norm of the column vectors are the moiré of moiré lengths, denoted as  $\lambda_{mn}^H$ . For  $m = n = 1$ , the moiré of moiré length  $\lambda_{11}^H$  is explicitly given as

$$\lambda_{11}^H = \frac{(1 + \delta)a_M^{12}}{\sqrt{2(1 + \delta)(1 - \cos \phi) + \delta^2}}, \quad (\text{S4})$$

where  $\phi = \cos^{-1}\left(\frac{\mathbf{a}_1^{(12)} \cdot \mathbf{a}_1^{(23)}}{|\mathbf{a}_1^{(12)}| |\mathbf{a}_1^{(23)}|}\right)$  is the twist angle between the bilayer moiré supercells and  $\delta = \frac{\sin \theta_{23}}{\sin \theta_{12}} - 1$  is the lattice mismatch between the two bilayer moiré supercells such that  $a_M^{23} = (1 + \delta)a_M^{12}$ . Equation (S4) agrees with the first-order approximation for the moiré length for a twisted bilayer with a lattice mismatch [S3], with the lattice constant being the bilayer moiré length between L1 and L2.

A dominant moiré of moiré length does not necessarily exist nor evolve smoothly under the continuous change of the twist angle. To see this, we will consider different harmonics of the higher-order moiré patterns. To find the dominant harmonic for an arbitrary pair of twist angles, we calculate  $A_{mn}^H$  for  $|m|, |n| \leq 15$  numerically and find the  $(m, n)$  such that the norm of  $G_{mn}^H$  is the smallest, or, equivalently, that the moiré of moiré length  $\lambda_{mn}$  is largest. We are neglecting the cases where higher order harmonics dominate, such as the cases where  $\theta_{12}$  and  $\theta_{23}$  are different by more than a factor of 15. In those cases, the two bilayers moiré supercells have very different sizes and become essentially decoupled, which is not the focus of our study. Figure S2(a) shows the moiré of moiré harmonics for varying  $\theta_{12}$  at a fixed  $\theta_{23} = 2.8^\circ$ , indicating the non-smooth dependence of the dominant moiré of moiré length on the twist angle. In tTLG, there exists a supercell approximation when there is a clear dominant harmonic, that is when  $\theta_{12} \approx N\theta_{23}$  or  $\theta_{23} \approx N\theta_{12}$  for  $N \in \mathbb{Z}$ . For example, at  $\theta_{12} = 2.6^\circ, \theta_{23} = 2.8^\circ$ , the dominant harmonic is (1, 1) [see Fig. S2(b)] and at  $\theta_{12} = 1.35^\circ, \theta_{23} = 2.8^\circ$ , the dominant harmonic is (2, 1) [see Fig. S2(d)]. However, there are cases where there is no clear dominant moiré of moiré. For example, in Fig. S2(c), it is difficult to visually discern a large repeating pattern and the estimated moiré of moiré lattice vectors fail to capture the relevant length scale. This is because near  $\theta_{12} = 1.8^\circ$ , many harmonics, such as (3, 2), (5, 4), and (5, 3), all have comparable lengths [see Fig. S2(a) the corresponding point].

## II. MOMENTUM-SPACE MODEL

In this section, we offer a detailed derivation of our momentum-space model and density of states formalism, and study the convergence as a function of the momentum space cutoff radius.



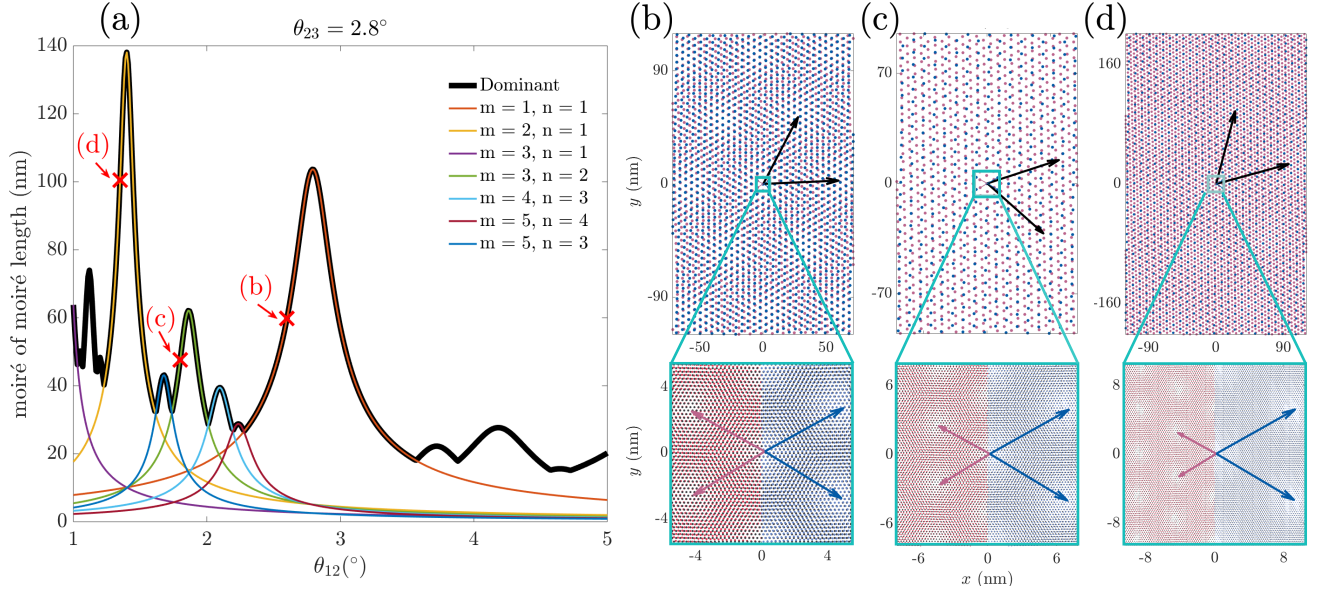


FIG. S2: (a) Moiré of moiré of lengths  $\lambda_{mn}^H$  as a function of  $\theta_{12}$  for  $\theta_{23} = 2.8^\circ$ . Each color corresponds to a different set of  $(m, n)$ . The thick black line indicates the dominant length. (b)-(d) Examples moiré of moiré geometries, corresponding to the red crosses in (a). Top: red and blue scattered points are the lattice points of the bilayer moiré supercells between L1-L2 and L2-L3 respectively. Due to the different twist angles, the moiré lattice vectors are slightly rotated and have different lattice constants. Black vectors indicate estimated dominant moiré of moiré supercell lattice vectors. A blowup of the small boxed area is shown below, with points representing the atomic positions of each monolayer graphene, for L1-L2 on the left half and for L2-L3 on the right half. Red and blue vectors are the bilayer moiré lattice vectors of L1-L2 and L2-L3 respectively.

### A. Detailed derivation of momentum-space model

To model the electronic structure of the tTLG system, we start from a tight-binding approximation for each individual layer; we take into account the interlayer hopping in a transverse tight-binding approximation between nearest neighbors. We start by writing the Hamiltonian for the trilayer as a sum of the following terms

$$H = \sum_{l=1}^3 H^\ell + \sum_{l=1,2} (V^{\ell, \ell+1} + V^{\ell+1, \ell}), \quad (\text{S5})$$

where  $H^\ell$  is the Hamiltonian for the  $\ell$ -th layer and  $V^{ij}$  describes the interlayer hopping. For simplicity, we only consider the interlayer couplings between adjacent layers. DFT calculations predict that the interlayer coupling between L1 and L3 is roughly 10 times smaller than the coupling between adjacent layers [e.g., between L1 and L2] [S4]. In a second quantized notation,  $H^\ell$  can be written as

$$H^\ell = -t \sum_{\mathbf{R}^{(\ell)}} c_{\ell, A}^\dagger(\mathbf{R}^{(\ell)}) [c_{\ell, B}(\mathbf{R}^{(\ell)}) + c_{\ell, B}(\mathbf{R}^{(\ell)} - \mathbf{a}_1^{(\ell)}) + c_{\ell, B}(\mathbf{R}^{(\ell)} - \mathbf{a}_2^{(\ell)})] + h.c., \quad (\text{S6})$$

where  $c_{\ell, \alpha}^\dagger$  and  $c_{\ell, \alpha}$  are the creation and annihilation fermionic operators of the orbital  $\alpha$  in layer  $l$ ,  $\mathbf{a}_{1,2}^{(\ell)}$  are the lattice vectors of layer  $l$ , and  $t$  is the hopping parameter between nearest neighbors. As for the interlayer coupling, we define the following overlap matrix element in the tight-binding basis

$$t_{\alpha\beta}^{ij}(\mathbf{R}^{(i)}, \mathbf{R}^{(j)}) = \langle i, \mathbf{R}^{(i)}, \alpha | H | j, \mathbf{R}^{(j)}, \beta \rangle, \quad (\text{S7})$$

where  $\alpha$  and  $\beta$  denotes the sublattice degree of freedom. The interlayer Hamiltonian in the second-quantized notation is

$$V^{ij} = \sum_{\mathbf{R}^{(i), \alpha}, \mathbf{R}^{(j), \beta}} c_{i, \alpha}^\dagger(\mathbf{R}^{(i)}) t_{\alpha\beta}^{ij}(\mathbf{R}^{(i)}, \mathbf{R}^{(j)}) c_{j, \beta}(\mathbf{R}^{(j)}). \quad (\text{S8})$$

We obtain the Hamiltonian in the momentum basis at a center site momentum  $\mathbf{k}$ . Defining  $\mathbf{Q}^{(\ell)} = \mathbf{k}^{(\ell)} + \mathbf{k}$  for  $\mathbf{k}^{(\ell)} \in \Gamma^{(\ell)*}$ . We perform the Fourier transform as follows

$$\begin{aligned} c_{\ell,\alpha}^\dagger(\mathbf{R}^{(\ell)}) &= \frac{1}{\sqrt{|\Gamma^{(\ell)*}|}} \int_{\Gamma^{(\ell)*}} d\mathbf{k}^{(\ell)} e^{i\mathbf{Q}^{(\ell)} \cdot (\mathbf{R}^{(\ell)} + \boldsymbol{\tau}_\alpha^{(\ell)})} c_{\ell,\mathbf{k}^{(\ell)},\alpha}^\dagger, \\ c_{\ell,\alpha}(\mathbf{R}^{(\ell)}) &= \frac{1}{\sqrt{|\Gamma^{(\ell)*}|}} \int_{\Gamma^{(\ell)*}} d\mathbf{k}^{(\ell)} e^{-i\mathbf{Q}^{(\ell)} \cdot (\mathbf{R}^{(\ell)} + \boldsymbol{\tau}_\alpha^{(\ell)})} c_{\ell,\mathbf{k}^{(\ell)},\alpha}, \end{aligned} \quad (\text{S9})$$

where the integral is over the Brillouin zone of the  $\ell$ -th layer,  $\boldsymbol{\tau}_A^{(\ell)} = \mathbf{0}$ ,  $\boldsymbol{\tau}_B^{(\ell)} = 1/3(\mathbf{a}_1^{(\ell)} + \mathbf{a}_2^{(\ell)})$ . The inverse of the transform in Eq. (S9) is

$$\begin{aligned} c_{\ell,\mathbf{k}^{(\ell)},\alpha}^\dagger &= \frac{1}{\sqrt{|\Gamma^{(\ell)*}|}} \sum_{\mathbf{R}^{(\ell)}} e^{-i\mathbf{Q}^{(\ell)} \cdot (\mathbf{R}^{(\ell)} + \boldsymbol{\tau}_\alpha^{(\ell)})} c_{\ell,\alpha}^\dagger(\mathbf{R}^{(\ell)}), \\ c_{\ell,\mathbf{k}^{(\ell)},\alpha} &= \frac{1}{\sqrt{|\Gamma^{(\ell)*}|}} \sum_{\mathbf{R}^{(\ell)}} e^{i\mathbf{Q}^{(\ell)} \cdot (\mathbf{R}^{(\ell)} + \boldsymbol{\tau}_\alpha^{(\ell)})} c_{\ell,\alpha}(\mathbf{R}^{(\ell)}), \end{aligned} \quad (\text{S10})$$

where  $|\Gamma^{(\ell)*}|$  is the area of the Brillouin zone in the  $\ell$ -th layer. The intralayer Hamiltonian in the Bloch basis can now be written as follows

$$\begin{aligned} H^\ell &= -\frac{t}{|\Gamma^{(\ell)*}|} \sum_{\mathbf{R}^{(\ell)}} \int_{\Gamma^{(\ell)*}} d\mathbf{k}^{(\ell)} \int_{\Gamma^{(\ell)*}} d\mathbf{k}'^{(\ell)} e^{i(\mathbf{k}^{(\ell)} - \mathbf{k}'^{(\ell)}) \cdot \mathbf{R}^{(\ell)}} \sum_{\mathbf{s}_i^{(\ell)}} e^{i\mathbf{k} \cdot \mathbf{s}_i^{(\ell)}} c_{\ell,\mathbf{k},A}^\dagger c_{\ell,\mathbf{k}'^{(\ell)},B} \\ &= -t \int_{\Gamma^{(\ell)*}} d\mathbf{k}^{(\ell)} \sum_{\mathbf{s}^{(\ell)}} e^{i\mathbf{Q}^{(\ell)} \cdot \mathbf{s}_i^{(\ell)}} c_{\ell,\mathbf{k}^{(\ell)},A}^\dagger c_{\ell,\mathbf{k}^{(\ell)},B}, \end{aligned} \quad (\text{S11})$$

where we use the Poisson summation formula,  $\sum_{\mathbf{R}^{(\ell)}} e^{i\mathbf{k}^{(\ell)} \cdot \mathbf{R}^{(\ell)}} = |\Gamma^{(\ell)*}| \sum_{\mathbf{G}^{(\ell)}} \delta_{\mathbf{k}^{(\ell)}, \mathbf{G}^{(\ell)}}$ . We also define  $\mathbf{s}_i^{(\ell)}$  to describe the nearest neighbor separation between  $A$  and  $B$  sublattices, which are given as  $\mathbf{s}_1^{(\ell)} = 1/3(\mathbf{a}_1^{(\ell)} + \mathbf{a}_2^{(\ell)})$ ,  $\mathbf{s}_2^{(\ell)} = 1/3(-2\mathbf{a}_1^{(\ell)} + \mathbf{a}_2^{(\ell)})$ ,  $\mathbf{s}_3^{(\ell)} = 1/3(\mathbf{a}_1^{(\ell)} - 2\mathbf{a}_2^{(\ell)})$ . The intralayer Hamiltonian in the basis of  $c_{\ell,\mathbf{k}^{(\ell)},\alpha}$  can then be written as

$$H^\ell(\mathbf{Q}^{(\ell)}) = -t \begin{bmatrix} 0 & f_\ell(\mathbf{Q}^{(\ell)}) \\ f_\ell^*(\mathbf{Q}^{(\ell)}) & 0 \end{bmatrix}, \quad (\text{S12})$$

where  $f_\ell(\mathbf{Q}^{(\ell)}) = \sum_{\mathbf{s}_i^{(\ell)}} e^{i\mathbf{Q}^{(\ell)} \cdot \mathbf{s}_i^{(\ell)}}$ . The Hamiltonian is equivalent to the monolayer graphene tight-binding model at a given momentum  $\mathbf{Q}^{(\ell)}$  [S5]. For the intralayer Hamiltonian, there is no constraint on  $\mathbf{Q}^{(\ell)}$ .

Similarly, we write the interlayer Hamiltonian in the  $c_{\ell,\mathbf{k}^{(\ell)},\alpha}^\dagger$  basis

$$V^{ij} = \int_{\Gamma^{(i)*}} d\mathbf{k}^{(i)} \int_{\Gamma^{(j)*}} d\mathbf{k}^{(j)} \sum_{\alpha\beta} c_{i,\mathbf{k}^{(i)},\alpha}^\dagger T_{ij}^{\alpha\beta}(\mathbf{k}^{(i)}, \mathbf{k}^{(j)}) c_{j,\mathbf{k}^{(j)},\beta}, \quad (\text{S13})$$

where we use Eq. (S9) and

$$T_{\alpha\beta}^{ij}(\mathbf{k}^{(i)}, \mathbf{k}^{(j)}) = \frac{1}{\sqrt{|\Gamma^{(i)*}| |\Gamma^{(j)*}|}} \sum_{\mathbf{R}^{(i)}, \mathbf{R}^{(j)}} e^{i\mathbf{Q}^{(i)} \cdot (\mathbf{R}^{(i)} + \boldsymbol{\tau}_\alpha^{(i)})} t_{\alpha\beta}^{ij}(\mathbf{R}^{(i)}, \mathbf{R}^{(j)}) e^{-i\mathbf{Q}^{(j)} \cdot (\mathbf{R}^{(j)} + \boldsymbol{\tau}_\beta^{(j)})}. \quad (\text{S14})$$

We now apply the two center approximation

$$t_{\alpha\beta}^{ij}(\mathbf{R}^{(i)}, \mathbf{R}^{(j)}) = t_{\alpha\beta}^{ij}(\mathbf{R}^{(i)} + \boldsymbol{\tau}_\alpha^{(i)} - \mathbf{R}^{(j)} - \boldsymbol{\tau}_\beta^{(j)}), \quad (\text{S15})$$

and write the interlayer coupling in terms of a two-dimensional Fourier Transform

$$\begin{aligned} t_{\alpha\beta}^{ij}(\mathbf{R}^{(i)}, \mathbf{R}^{(j)}) &= t_{\alpha\beta}^{ij}(\mathbf{R}^{(i)} + \boldsymbol{\tau}_\alpha^{(i)} - \mathbf{R}^{(j)} - \boldsymbol{\tau}_\beta^{(j)}) \\ &= \int \frac{d\mathbf{p}}{(2\pi)^2} e^{i\mathbf{p} \cdot (\mathbf{R}^{(i)} + \boldsymbol{\tau}_\alpha^{(i)} - \mathbf{R}^{(j)} - \boldsymbol{\tau}_\beta^{(j)})} \tilde{t}_{\alpha\beta}^{ij}(\mathbf{p}). \end{aligned} \quad (\text{S16})$$

Plugging Eq. (S16) into Eq. (S14), the interlayer coupling matrix element in momentum space is

$$\begin{aligned}
T_{\alpha\beta}^{ij}(\mathbf{k}^{(i)}, \mathbf{k}^{(j)}) &= \frac{1}{\sqrt{|\Gamma^{(i)*}||\Gamma^{(j)*}|}} \int \frac{d\mathbf{p}}{(2\pi)^2} \sum_{\mathbf{R}^{(i)}, \mathbf{R}^{(j)}} e^{i(\mathbf{Q}^{(i)}+\mathbf{p})\cdot(\mathbf{R}^{(i)}+\boldsymbol{\tau}_{\alpha}^{(i)})} t_{\alpha\beta}^{ij}(\mathbf{p}) e^{-i(\mathbf{Q}^{(j)}+\mathbf{p})\cdot(\mathbf{R}^{(j)}+\boldsymbol{\tau}_{\beta}^{(j)})} \\
&= \sqrt{|\Gamma^{(i)*}||\Gamma^{(j)*}|} \sum_{\mathbf{G}^{(i)}, \mathbf{G}^{(j)}} \int \frac{d\mathbf{p}}{(2\pi)^2} e^{i\mathbf{G}^{(i)}\cdot\boldsymbol{\tau}_{\alpha}^{(i)}} \tilde{t}_{\alpha\beta}^{ij}(\mathbf{p}) e^{-i\mathbf{G}^{(j)}\cdot\boldsymbol{\tau}_{\beta}^{(j)}} \delta_{\mathbf{k}+\mathbf{k}^{(i)}-\mathbf{p}, \mathbf{G}^{(i)}} \delta_{\mathbf{k}+\mathbf{k}^{(j)}-\mathbf{p}, \mathbf{G}^{(j)}} \\
&= \frac{1}{|\Gamma|} \sum_{\mathbf{G}^{(i)}, \mathbf{G}^{(j)}} e^{i\mathbf{G}^{(i)}\cdot\boldsymbol{\tau}_{\alpha}^{(i)}} \tilde{t}_{\alpha\beta}^{ij}(\mathbf{k}^{(i)} + \mathbf{k} - \mathbf{G}^{(i)}) e^{-i\mathbf{G}^{(j)}\cdot\boldsymbol{\tau}_{\beta}^{(j)}} \delta_{\mathbf{k}^{(i)}-\mathbf{G}^{(i)}, \mathbf{k}^{(j)}-\mathbf{G}^{(j)}}. \tag{S17}
\end{aligned}$$

In the last step, we use the Poisson summation rule and  $|\Gamma^{(\ell)*}| = 4\pi^2|\Gamma|^{-1}$ , where  $|\Gamma|$  is the monolayer unit cell area. We have obtained the scattering selection rule  $\mathbf{k}^{(i)} - \mathbf{G}^{(i)} = \mathbf{k}^{(j)} - \mathbf{G}^{(j)}$  for  $i = j \pm 1$ , which imposes the constraint on the values of allowed  $\mathbf{k}^{(\ell)}$ .

Combining the intralayer and interlayer terms, the Hamiltonian in the  $c_{\ell, \mathbf{k}^{(\ell)}, \alpha}^{\dagger}$  basis can be represented as a  $3 \times 3$  block given in Eq. (1) of the main text.

## B. Low-energy limit

We can greatly simplify the model by taking the low-energy limit. Each  $H^{\ell}$  can be expanded around its Dirac point,  $\mathbf{k}^{(\ell)} = K_{L\ell} + \mathbf{q}^{(\ell)}$ , as a rotated Dirac Hamiltonian  $H_D^{\ell}(\mathbf{q})$  for  $\mathbf{q} = \mathbf{k} + \mathbf{k}^{(\ell)} - K_{L\ell}$ :

$$\begin{aligned}
H^1(\mathbf{k}) &\approx H_D^1(\mathbf{q}) = v_F \begin{bmatrix} 0 & e^{i\theta_{12}} q_+ \\ e^{-i\theta_{12}} q_- & 0 \end{bmatrix}, \\
H^2(\mathbf{k}) &\approx H_D^2(\mathbf{q}) = v_F \begin{bmatrix} 0 & q_+ \\ q_- & 0 \end{bmatrix}, \\
H^3(\mathbf{k}) &\approx H_D^3(\mathbf{q}) = v_F \begin{bmatrix} 0 & e^{-i\theta_{23}} q_+ \\ e^{i\theta_{23}} q_- & 0 \end{bmatrix}, \tag{S18}
\end{aligned}$$

where  $q_{\pm} = q_x \pm iq_y$ . For the interlayer coupling, we substitute  $\mathbf{k}^{(\ell)} = \mathbf{q}^{(\ell)} + K_{L\ell}$  into Eq. (S17),

$$T_{\alpha\beta}^{ij}(\mathbf{q}^{(i)}, \mathbf{q}^{(j)}) = \frac{1}{|\Gamma|} \sum_{\mathbf{G}^{(i)}, \mathbf{G}^{(j)}} e^{i\mathbf{G}^{(i)}\cdot\boldsymbol{\tau}_{\alpha}^{(i)}} \tilde{t}_{\alpha\beta}^{ij}(\mathbf{k} + K_{Li} + \mathbf{q}^{(i)} + \mathbf{G}^{(i)}) e^{-i\mathbf{G}^{(j)}\cdot\boldsymbol{\tau}_{\beta}^{(j)}} \delta_{\mathbf{q}^{(i)}+K_{Li}-\mathbf{G}^{(i)}, \mathbf{q}^{(j)}+K_{Lj}-\mathbf{G}^{(j)}}. \tag{S19}$$

For momenta near the Dirac point, since  $|\mathbf{q}^{(i)}|, |\mathbf{k}| \ll |K_{Li}|, |\mathbf{G}^{(i)}|$  we can approximate  $\tilde{t}_{\alpha\beta}^{ij}(\mathbf{k} + K_{Li} + \mathbf{q}^{(i)} + \mathbf{G}^{(i)}) \approx \tilde{t}_{\alpha\beta}^{ij}(K_{Li} + \mathbf{G}^{(i)})$ . This approximation can lead to the suppression of particle-hole asymmetry in the tight-binding model [S6, S7]. Due to the rapid decay of the hopping parameter  $\tilde{t}(\mathbf{p})$  as  $\mathbf{p}$  increases [S8], we keep only the first shell in the summation in Eq. (S19):

$$T_{\alpha\beta}^{ij}(\mathbf{q}^{(i)}, \mathbf{q}^{(j)}) = \sum_{n=1}^3 T_{n, \alpha\beta}^{ij} \delta_{\mathbf{q}^{(i)}-\mathbf{q}^{(j)}, -\mathbf{q}_n^{ij}}, \tag{S20}$$

where  $\mathbf{q}_1^{ij} = K_{Li} - K_{Lj}$ ,  $\mathbf{q}_2^{ij} = \mathcal{R}^{-1}(2\pi/3)\mathbf{q}_1^{ij}$ , and  $\mathbf{q}_3^{ij} = \mathcal{R}(2\pi/3)\mathbf{q}_1^{ij}$  (see Fig. S1b). We include out-of-plane relaxation by letting  $t_{AA}^{ij} = t_{BB}^{ij} = \omega_0 = 0.07$  eV and  $t_{AB}^{ij} = t_{BA}^{ij} = \omega_1 = 0.11$  eV, which matches with the interlayer coupling in Nam and Koshino [S9] and Carr *et al.* [S6]. In matrix form,

$$T_1^{ij} = \begin{bmatrix} \omega_0 & \omega_1 \\ \omega_1 & \omega_0 \end{bmatrix}, T_2^{ij} = \begin{bmatrix} \omega_0 & \omega_1 \bar{\phi} \\ \omega_1 \phi & \omega_0 \end{bmatrix}, T_3^{ij} = \begin{bmatrix} \omega_0 & \omega_1 \phi \\ \omega_1 \bar{\phi} & \omega_0 \end{bmatrix}, \tag{S21}$$

where  $\phi = \exp(i\frac{2\pi}{3})$ ,  $\bar{\phi} = \exp(-i\frac{2\pi}{3})$ .

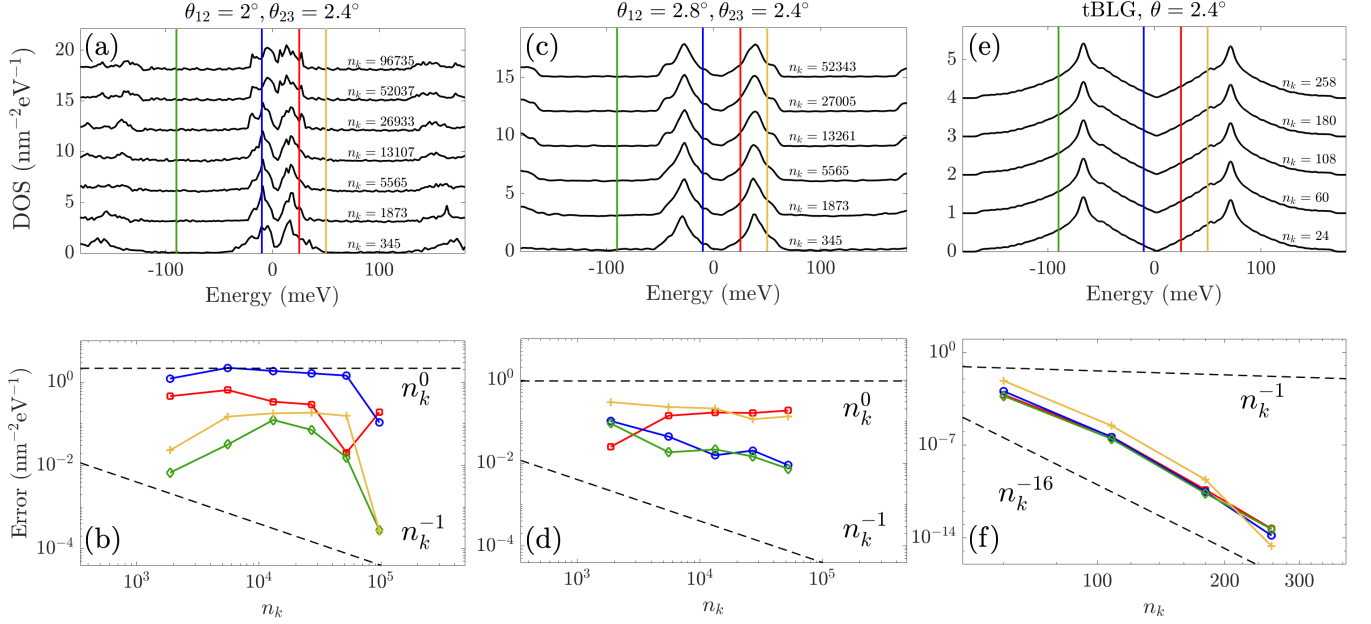


FIG. S3: Top: DOS obtained using different sizes of momentum-space basis,  $n_k$ . Bottom: errors in the DOS corresponding to the vertical lines on the top with the same color. The error is defined as the difference between the DOS value at the given energy and the DOS at the largest cutoff shown on the top. The dashed lines are guides to the eyes showing power law scaling of the error as a function of  $n_k$ .

### C. Density of States

The DOS at a given energy  $\epsilon$ ,  $\mathcal{D}(\epsilon)$ , for an incommensurate tight-binding model is defined as [S10]

$$\mathcal{D}(\epsilon) = \sum_r \frac{1}{N} \sum_{n=1}^N \delta(\epsilon - \epsilon_n) |\psi_n(r)|^2, \quad (\text{S22})$$

where the  $r$  sum is over all real space lattice positions,  $n$  is the band index, and  $\psi_n(r)$  is the corresponding eigenfunction. To obtain the DOS numerically, we use a Gaussian function  $\phi_{\epsilon, \kappa}(x) = \frac{2\sqrt{\ln 2}}{\sqrt{\pi}\kappa} \exp\left[-4 \ln 2 \frac{(x-\epsilon)^2}{\kappa^2}\right]$  to approximate the  $\delta$  function, and  $\kappa$  is the full-width-half-maximum of the Gaussian, which determines the energy resolution of the DOS [S11]. We can transform the DOS equation to momentum space:

$$\mathcal{D}(\epsilon) = \frac{\mathcal{N}}{2} \sum_{\alpha=A,B} \sum_{\ell=1,2} \int_{\Gamma^{(\ell, \ell+1)*}} \sum_n \phi_{\epsilon, \kappa}(\epsilon_{n, \mathbf{k}}) |\psi_{n, \mathbf{k}}|^2 d\mathbf{k}, \quad (\text{S23})$$

where  $\mathcal{N}$  is a normalization constant,  $\epsilon_{n, \mathbf{k}}$  is an energy within the energy window  $[\epsilon - \Delta\epsilon/2, \epsilon + \Delta\epsilon/2]$ ,  $\Delta\epsilon$  is the energy interval,  $\psi_{n, \mathbf{k}}$  and  $\epsilon_{n, \mathbf{k}}$  is an eigen-pair of the Hamiltonian  $\mathcal{H}(\mathbf{k})$  in Eq. (1) of the main text associated with the center site  $\mathbf{k}$  and band  $n$ . The integral is evaluated over the bilayer moiré Brillouin zone between layers  $\ell$  and  $\ell + 1$ ,  $\Gamma^{(\ell, \ell+1)*}$ , and we discretize  $\Gamma^{(\ell, \ell+1)*}$  using a  $22 \times 22$  grid to evaluate the integral. We adapt  $\kappa$  based on the area of the integration domain  $\Gamma^{(\ell, \ell+1)*}$  as  $\theta_{\ell, \ell+1}$  changes.

In order to make a direct comparison between the DOS at different twist angles, we need to properly normalize the DOS. For a given cutoff radius, we first calculate the DOS of the intralayer Hamiltonian only, which reduces to three independent copies of monolayer graphene. Near the charge-neutrality point, the DOS per eV per  $\text{nm}^2$  is given by [S5]

$$\mathcal{D}(\epsilon) = \frac{6}{\pi} \frac{|\epsilon|}{v_F^2}, \quad (\text{S24})$$

where the prefactor includes a factor 3 from the number of layers as well as a factor of 4 from spin and valley degeneracies. We then obtain a normalization constant by fixing the prefactor to the expected slope given in Eq. (S24)



Figure S4(a) shows the  $v_F^*$  to  $v_F$  ratio as a function of  $\theta_{12}$  at a few values of  $\theta_{23}$ . As  $\theta_{23}$  increases, the  $v_F^*/v_F$  ratio approaches the tBLG curve. Figure S4(b) shows  $v_F^*/v_F$  for equal twist angles, which shows that perturbation theory predicts that  $v_F^*$  can still go to zero at  $1.72^\circ$ . However, in our numerical calculation using the full Hamiltonian, we do not observe a complete flattening of bands at this twist angle.

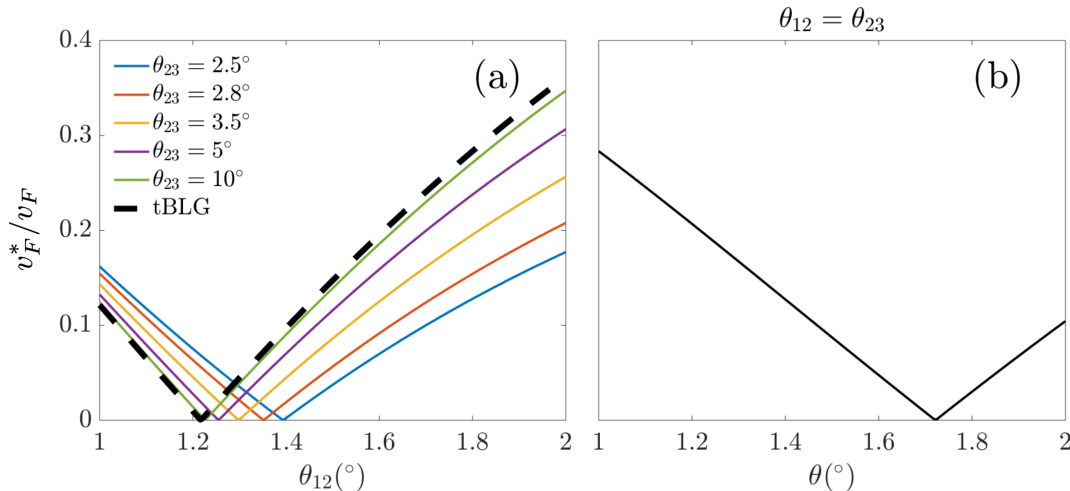


FIG. S4: (a) The ratio of renormalized Fermi velocity  $v_F^*$  to the monolayer Fermi velocity  $v_F$  as a function of  $\theta_{12}$  for given values of  $\theta_{23}$ . Black dashed line shows the tBLG  $v_F^*/v_F$  ratio. (b)  $v_F^*/v_F$  ratio as a function of twist angle for  $\theta_{12} = \theta_{23}$ .

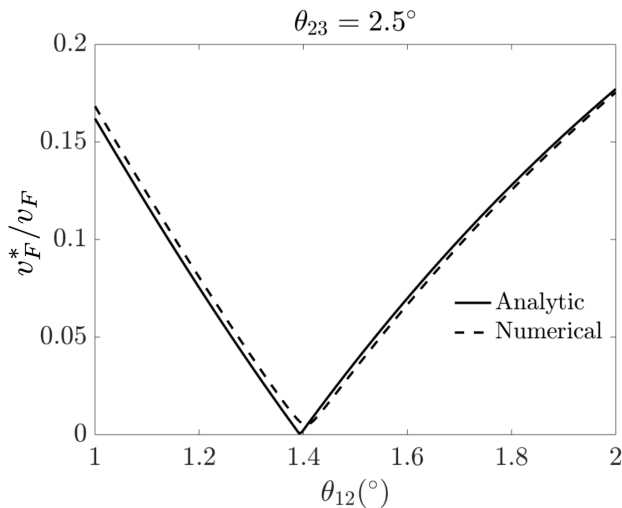


FIG. S5: Comparison between the renormalized Fermi velocity  $v_F^*$  of the Hamiltonian in Eq. (S25) calculated analytically (solid line) and numerically (dashed line).

Finally, we show that our assumption in the analytic calculation of an unrotated Dirac Hamiltonian for the intralayer Hamiltonian and  $\omega_0 = \omega_1$  does not significantly change the magic angle estimate. Figure S5 compares the  $v_F^*$  obtained analytically and numerically and show that the two curves and the magic angle do not differ significantly. In the numerical calculation, we diagonalize the  $14 \times 14$  Hamiltonian with rotated Dirac equation for the intralayer terms and  $\omega_0 = 0.07 \text{ eV}$ ,  $\omega_1 = 0.11 \text{ eV}$  for the interlayer terms. At  $\theta_{23} = 2.5^\circ$ , the magic angle obtained analytically and numerically differ by 1.1%.

#### IV. COMPARISON TO OTHER MODELS

In this section, we compare our results to two other works [S1, S2]. We first compare our results with the model proposed by Mora *et al.* [S1] and use it to gain further insights into our findings. In this alternate model, a different

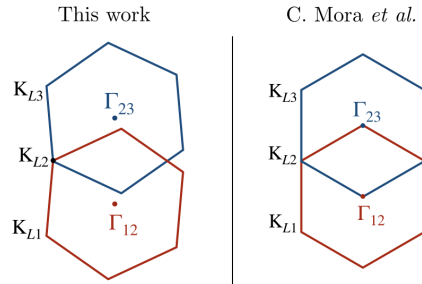


FIG. S6: Comparison of the bilayer moiré Brillouin zone geometry between our model and Mora *et al.* [S1] model with  $\theta_{12} = \theta_{23}$ . Left: two bilayer moiré Brillouin zones are misaligned by a small twist angle; right: the two bilayer moiré Brillouin zones are approximated to be aligned.

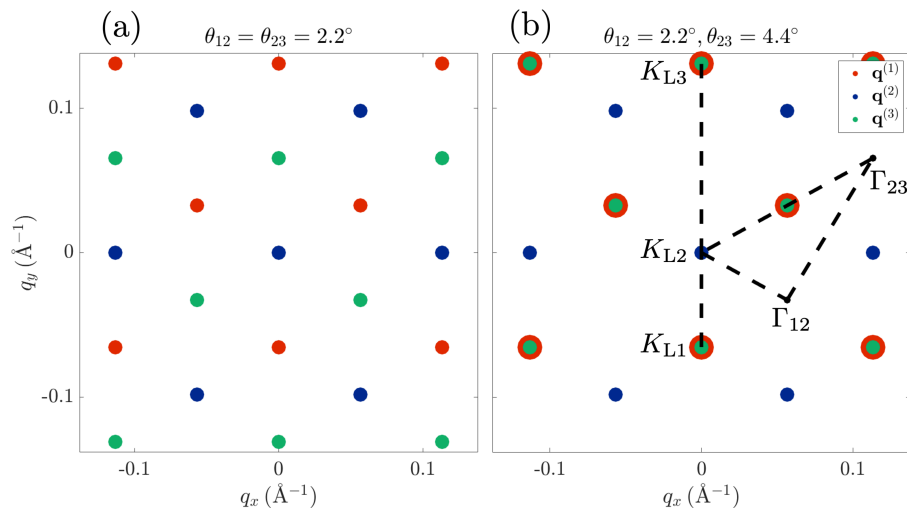


FIG. S7: The momentum degrees of freedom in the low-energy limit of the simplified model for (a)  $\theta_{12} = \theta_{23}$  and (b)  $2\theta_{12} = \theta_{23}$  with high symmetry points.

momentum-space basis is used by aligning the two bilayer moiré Brillouin zones [Fig. S6]. This approximation ignores the incommensurability of the system, making a two-dimensional momentum space crystal with the periodicity of the bilayer moiré Brillouin zone. As a result, the problem's complexity reduces to that of a bilayer. Formally, the Hamiltonian can still be written as the  $3 \times 3$  block as in Eq. (1) in the main text, but the size of the basis is reduced to be on the same order as tBLG. We implemented two cases: (1)  $\theta_{12} = \theta_{23}$  and (2)  $2\theta_{12} = \theta_{23}$ . Figure S7 shows the momentum-space basis for these two cases. In case (2), the larger bilayer Brillouin zone (L1-L2) is folded onto the smaller Brillouin zone (L2-L3) in momentum space. This model essentially describes a system consisted of  $2 \times 2$  L1-L2 moiré supercell and a L2-L3 moiré supercell. Figure S9 shows a comparison between the DOS obtained from the two models. We keep the values of  $\omega_0$  and  $\omega_1$  the same as our model and use the same approach to normalize the DOS for a direct comparison. We cut off the basis at the 4<sup>th</sup> shell and use a grid size  $22 \times 22$  for the density of states. The Gaussian FWHM we use is 5 meV for  $\theta < 2^\circ$  and 8 meV for  $\theta \geq 2^\circ$ , where  $\theta$  is the twist angle that determines the size of the Brillouin zone.

For  $\theta_{12} = \theta_{23}$ , Fig. S8(a) shows the DOS obtained with the simplified model, which agrees qualitatively with the DOS from our model [Fig. 3(a) of the main text]. However, here the DOS has the sharpest peak between  $1.7^\circ$  and  $1.8^\circ$ , and at  $2.1^\circ$  the VHS have a larger width compared to our model. Figure S8(b)-(d) shows that the location of peaks away from the CNP are also very different from our model.

For  $2\theta_{12} = \theta_{23}$ , the two models predict similar trend for the VHS evolution, and the simplified model makes the right prediction for the magic angle. This is expected from perturbation theory, since the magic angle condition does

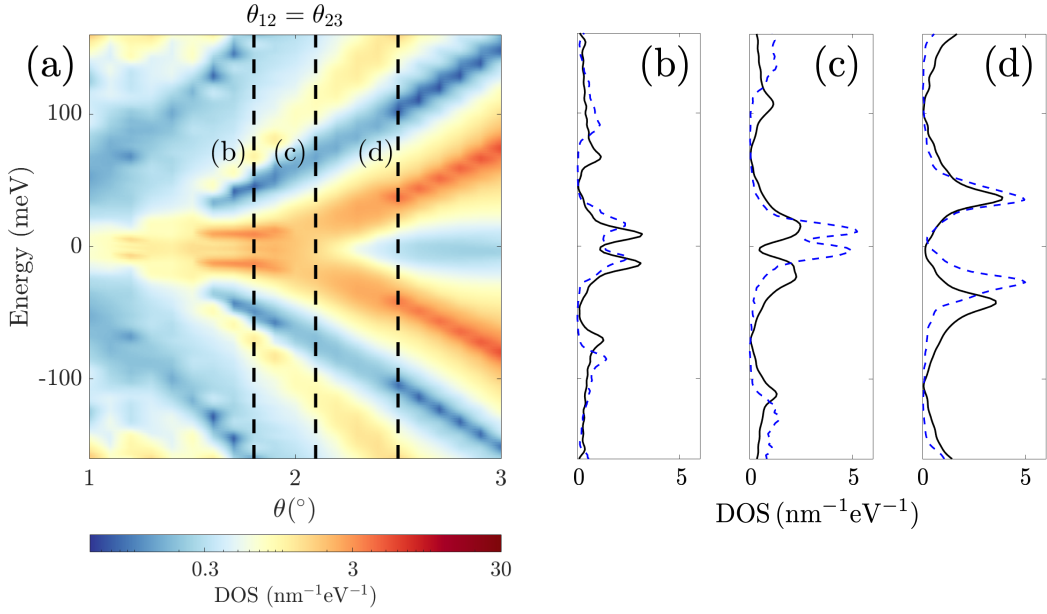


FIG. S8: DOS obtained with the Mora *et al.* [S1] model DOS on a logarithmic color scale at equal twist angles (same color scale as Fig. 3(a) in the main text for a direct comparison) (b)-(d) DOS states along the black dashed line in (a) for (b)  $\theta = 1.8^\circ$ , (c)  $\theta = 2.1^\circ$ , (d)  $\theta = 2.5^\circ$ , where the black solid lines are obtained using the Mora *et al.* [S1] model, and the blue dashed lines are obtained using our full model.

not rely on the existence of a moiré of moiré cell [as was shown in Section III]. However, the magnitude of the DOS differs significantly between the two models. This is because there are two flat bands near the CNP in the simplified model, whereas in our full model, there is a large number of nearly overlapping flat bands due to incommensurability [Fig. S10]. Figure S10 compares the band structure from our model and the simplified model. The two band structures are qualitatively similar but our model shows a large number of bands due to the lack of a periodic Brillouin zone. Furthermore, the aligned-bilayer approximation will exclude correlated phases that depend on band-hybridization or symmetries from the moiré of moiré length scale. Note that we do not plot the relative layer weights (color) of the band structure in the simplified model because of the way that the Brillouin zone is wrapped – the L1 degrees of freedom are wrapped on top of the L3 degrees of freedom. Therefore, the wavefunction weights from the two models are not directly comparable for this particular high symmetry line cut.

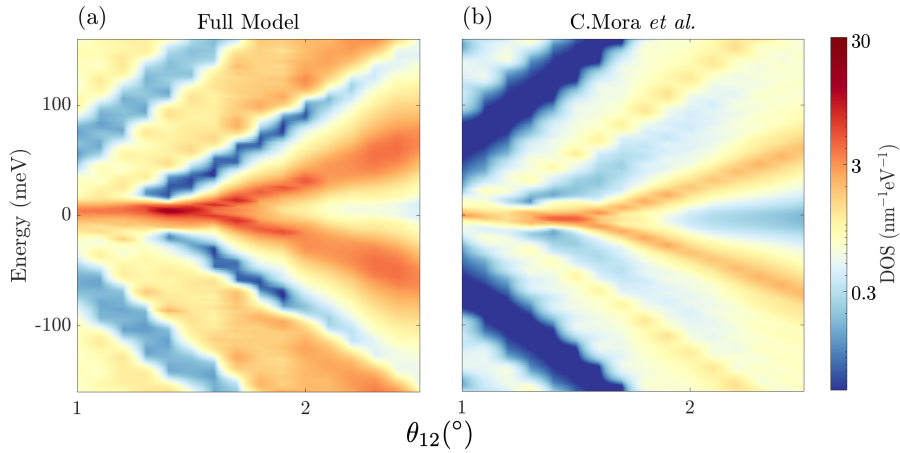


FIG. S9: DOS as a function of  $\theta_{12}$  with  $2\theta_{12} = \theta_{23}$  using (a) our full model and (b) the Mora *et al.* [S1] model, both on a logarithmic color scale.

We can use these results to further support our argument of bilayer moiré hybridization at equal twist angles. In



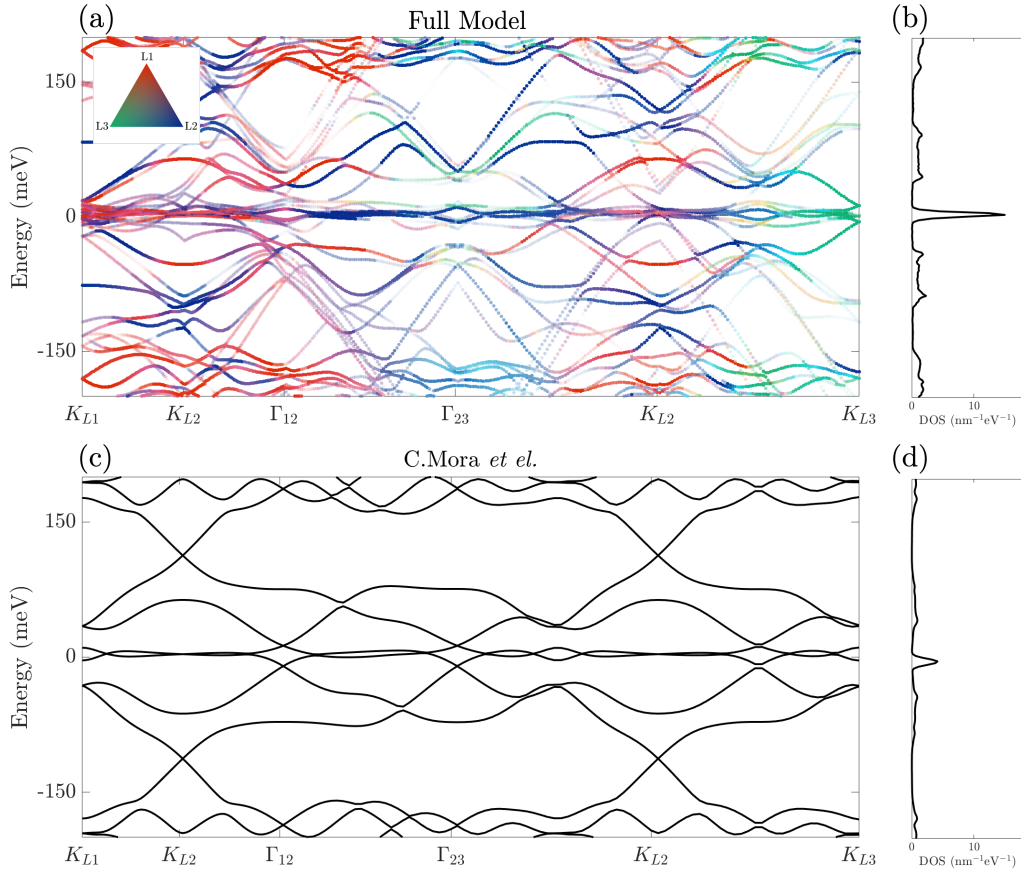


FIG. S10: Comparison of band structures and DOS at  $\theta_{12} = 1.4^\circ, \theta_{23} = 2.8^\circ$  between our model (top) along the green dashed line in Fig. S1(b) and the Mora *et al.* [S1] model (bottom) along the black dashed line in Fig. S7(b). In (a), colors represent the weight of the wavefunctions at the center site. Red, blue, and green represents weights purely from L1, L2, L3 respectively, and colors in between represent hybridization between different layers. A colormap is provided on the top left corner. The DOS from the two models are shown on the same scale.

this simplified model, sharpest VHS occur between  $1.7^\circ$  and  $1.8^\circ$ , which is in better agreement with the magic angle prediction from perturbation theory. In our model, the sharpest peak and the narrowest width occurs at a larger angle ( $2.1^\circ$ ). If this phenomenon is caused by moiré hybridization, the simplified model would not have it since it does not have the moiré of moiré scale. Indeed, the DOS from the two models differ most significantly at  $2.1^\circ$  [see Fig. S8(c)].

As we argue in the main text, adding electrons from the CNP at a low carrier concentration on the order of the tTLG moiré of moiré cells fills *one* flat band near the CNP in Fig. S10(a) at a time. Injecting electrons at a carrier concentration comparable to the bilayer moiré cell density would fill *all* these flat bands near the CNP. The simplified model can again be used to understand this argument. The model also predicts some band flattening at certain twist angles, but there are only two flat bands near the CNP [Fig. S10(c)]. Filling electrons to these two bands is equivalent to filling the bilayer moiré cell, since their momentum-space basis has the periodicity of bilayer moiré Brillouin zone and there is no moiré of moiré length in this model. These two flat bands near the CNP can be qualitatively considered as the limit where all the flat bands from our model overlap exactly on top of each other. Therefore, in terms of filling the supercell, filling the two flat bands from the simplified model is equivalent to filling all flat bands in the full model.

In addition to its inability to make predictions about electronic behaviors at the moiré of moiré scale, another major limitation of the model is its difficulty to generalize to arbitrary twist angles. For each set of twist angles on a different  $(m, n)$  harmonic, it requires the derivation of a new basis by folding the bilayer moiré Brillouin zone, while our model's basis is insensitive to the choice of angles and overcomes this limitation.

We can also use our model to study the case where L1 and L3 are twisted in the same direction (when  $\theta_{12}$  and  $\theta_{23}$  take opposite signs). This case has been studied theoretically by Amorim and Castro [S2] and its spectral properties have been investigated experimentally by Zuo *et al.* [S12]. Unlike our model, Amorim and Castro [S2] does not

take the low-energy limit [see Section II B]. Figure S11 shows the band structure and the corresponding DOS of  $\theta_{12} = -2.81^\circ, \theta_{23} = 2.1^\circ$  obtained with our model, which is the same case as Figs. 1(a) and 2 presented in Amorim and Castro [S2]. The results from the two models show an agreement, with the same VHS positions. The difference in the band structure can be most likely attributed to the different ways of truncating the momentum-space bases between the two models.

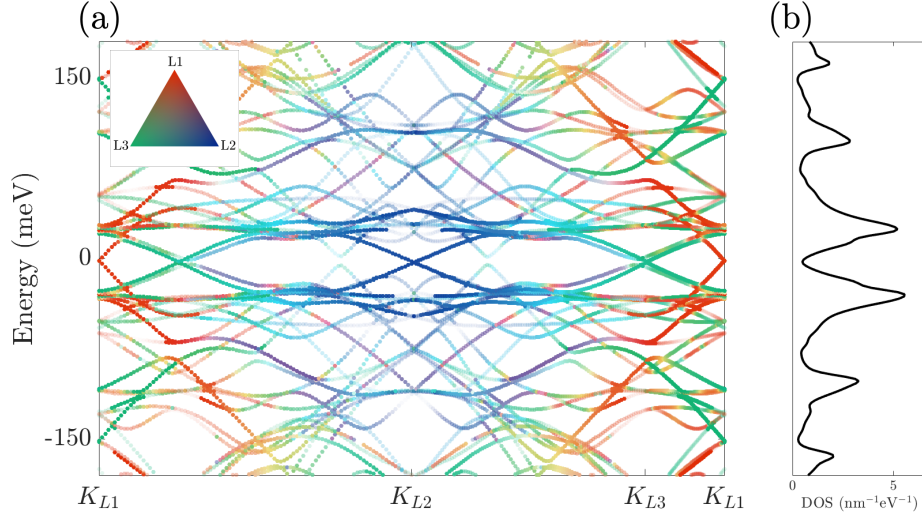


FIG. S11: (a) Band structure along a high symmetry line that connects the Dirac points of the three layers and (b) density of states at  $\theta_{12} = -2.81^\circ, \theta_{23} = 2.1^\circ$ . The colormap in (a) is the same as in Fig. S10(a).

- 
- [S1] Christophe Mora, Nicolas Regnault, and B. Andrei Bernevig, “Flatbands and Perfect Metal in Trilayer Moiré Graphene,” *Phys. Rev. Lett.* **123**, 026402 (2019).
- [S2] B. Amorim and Eduardo V. Castro, “Electronic spectral properties of incommensurate twisted trilayer graphene,” arXiv e-prints, arXiv:1807.11909 (2018), [arXiv:1807.11909 \[cond-mat.mes-hall\]](https://arxiv.org/abs/1807.11909).
- [S3] Matthew Yankowitz, Jiamin Xue, Daniel Cormode, Javier D. Sanchez-Yamagishi, K. Watanabe, T. Taniguchi, Pablo Jarillo-Herrero, Philippe Jacquod, and Brian J. Leroy, “Emergence of superlattice Dirac points in graphene on hexagonal boron nitride,” *Nature Physics* **8**, 382–386 (2012).
- [S4] Stephen Carr, Chenyuan Li, Ziyang Zhu, Efthimios Kaxiras, Subir Sachdev, and Alexander Kruchkov, “Ultraheavy and ultrarelativistic dirac quasiparticles in sandwiched graphenes,” *Nano Letters* **20**, 3030–3038 (2020).
- [S5] A. H. Castro Neto, F. Guinea, N. M. R. Peres, K. S. Novoselov, and A. K. Geim, “The electronic properties of graphene,” *Reviews of Modern Physics* **81**, 109–162 (2009).
- [S6] Stephen Carr, Shiang Fang, Ziyang Zhu, and Efthimios Kaxiras, “Exact continuum model for low-energy electronic states of twisted bilayer graphene,” *Physical Review Research* **1**, 013001 (2019).
- [S7] Shiang Fang, Stephen Carr, Ziyang Zhu, Daniel Massatt, and Efthimios Kaxiras, “Angle-Dependent *Ab initio* Low-Energy Hamiltonians for a Relaxed Twisted Bilayer Graphene Heterostructure,” arXiv e-prints, arXiv:1908.00058 (2019), [arXiv:1908.00058 \[cond-mat.mes-hall\]](https://arxiv.org/abs/1908.00058).
- [S8] Rafi Bistritzer and Allan H. MacDonald, “Moiré bands in twisted double-layer graphene,” *Proceedings of the National Academy of Science* **108**, 12233–12237 (2011).
- [S9] Nguyen N. T. Nam and Mikito Koshino, “Lattice relaxation and energy band modulation in twisted bilayer graphene,” *Phys. Rev. B* **96**, 075311 (2017).
- [S10] Stephen Carr, Daniel Massatt, Shiang Fang, Paul Cazeaux, Mitchell Luskin, and Efthimios Kaxiras, “Twistronics: Manipulating the electronic properties of two-dimensional layered structures through their twist angle,” *Phys. Rev. B* **95**, 075420 (2017).
- [S11] Daniel Massatt, Stephen Carr, Mitchell Luskin, and Christoph Ortner, “Incommensurate heterostructures in momentum space,” *Multiscale Modeling & Simulation* **16**, 429–451 (2018).
- [S12] Wei-Jie Zuo, Jia-Bin Qiao, Dong-Lin Ma, Long-Jing Yin, Gan Sun, Jun-Yang Zhang, Li-Yang Guan, and Lin He, “Scanning tunneling microscopy and spectroscopy of twisted trilayer graphene,” *Physical Review B* **97**, 035440 (2018).